Pontificia Universidad Católica de Chile
Facultad de Física
Instituto de Astrofísica

Period Change Rates of LMC Classical Cepheids using MESA

BY

Felipe Ignacio Espinoza Arancibia

Tesis presentada a la Facultad de Física de la Pontificia Universidad Católica de Chile, para optar al grado académico de Magíster en Astrofísica.

Supervisor : Dr. Márcio Catelan
Correctors : Dr. Alejandro Clocchiatti
Dr. Marc Pinsonneault

September, 2021
Santiago, Chile

Declaration

The work described in this thesis was undertaken between 2018 and 2021 while the author was a researcher master student under the supervision of Professor Márcio Catelan, in the Institute of Astrophysics at the Pontificia Universidad Católica de Chile. This work has not been submitted for any other degree at the Pontificia Universidad Católica de Chile or any other university.

Para mi familia

Acknowledgements

My deepest gratitude to Professor Márcio Catelan, who guided me during this journey. His knowledge and kindness made him an example to follow and helped me to improve as an astronomer and a person. Thanks to Gergely Hajdu and Nicolás Rodríguez, for their valuable comments on this work. Special thanks to my parents Ana María and Hernán, my sister Francisca, my aunts Julia and Isabel, and my grandmothers Mafalda and Esminda, for their constant support and love. I am grateful for the company of my friends Daniel and Matías, who have always been there for me. To my office mates: Carlos, Camila, Cesar, Jonathan and Pascal who have always been pleasant companions during working hours. To Junior, Panda and Oscar, who have made me smile every day. And I thank all those people who exchanged a kind conversation.

Support for this work has been provided by ANID's Millennium Science Initiative through grant ICN12_12009, awarded to the Millennium Institute of Astrophysics (MAS); by Proyecto Basal AFB-170002; and by FONDECYT grant #1171273.

Contents

List of Tables

List of Figures

Resumen

Las estrellas pulsantes, como las Cefeidas o las RR Lyrae, nos ofrecen una ventana para medir y estudiar los cambios debidos a la evolución estelar. Los cambios evolutivos en la densidad de la estrella producen cambios en el periodo de pulsación, que tienen un efecto acumulativo en los tiempos observados del brillo máximo o mínimo de la estrella. Por esta razón, las estrellas pulsantes son laboratorios de astrofísica estelar. En esta tesis calculamos un conjunto de modelos evolutivos de estrellas con 4 a 7 $M_\odot$ utilizando el código de evolución estelar *Modules for Experiments in Stellar Astrophysics* (MESA), variando la tasa de rotación inicial y la metalicidad. Durante la fase de quema de helio, la luminosidad aumenta a medida que aumenta la rotación, mientras que variando la metalicidad el comportamiento de la luminosidad resulta no monotónico. Por otro lado, la extensión del *blue loop* muestra una dependencia con la masa y la rotación más compleja. La extensión del blue loop para estrellas con $M \leq 5{,}5\, M_\odot$ disminuye a medida que aumenta la tasa de rotación, mientras que el comportamiento es no monotónico para estrellas con $M > 5{,}5\, M_\odot$. Debido a la pérdida de momento angular durante la fase de quema de hidrógeno en una cáscara, las Cefeidas no alcanzan rotaciones cercanas a la rotación crítica.

Utilizando *Radial Stellar Pulsations* (RSP), la nueva funcionalidad de MESA, obtuvimos los bordes de la banda de inestabilidad (IS) y los periodos lineales para el modo fundamental. Se obtuvieron relaciones período-edad, período-edad-temperatura, período-luminosidad y período-luminosidad-temperatura para tres tasas de rotación y metalicidades, que mostraron dependencias con el número de cruce, la posición en la IS, la

rotación y la metalicidad. Las tasas de cambio de periodo se calcularon directamente a partir de los periodos lineales. Los modelos durante el segundo cruce mostraron una dependencia no monontónica con la rotación, mientras que los modelos sin rotación muestran una mayor tasa de cambio de periodo durante el tercer cruce. Al variar el contenido de metales, los modelos con mayor metalicidad presentan una tasa ligeramente superior durante el segundo cruce.

Comparamos nuestros modelos con los trabajos presentados en la literatura utilizando el código de Ginebra. Encontramos grandes diferencias entre los modelos dada la diferente implementación de la rotación entre los códigos. Además, comparamos nuestras tasas de cambio de periodo con las calculadas en trabajos recientes en la literatura, para las cefeidas de La Gran Nube de Magallanes (LMC). Encontramos un buen acuerdo en general, ya que 72,2% de los datos caen dentro de rango de 3-sigma de los modelos. La implementación de procesos aún no incluidos en MESA, como la pérdida de masa impulsada por la pulsación, podría ayudarnos a cubrir mejor las tasas de cambio de periodo empíricas en la literatura.

Abstract

Pulsating stars such as Cepheids or RR Lyrae offer us a window to measure and study changes due to stellar evolution. Evolutionary changes in the star's density will produce changes in the pulsation period, which will have a cumulative effect on the observed times of the star's maximum or minimum brightness. For this reason, classical pulsators are laboratories for stellar astrophysics. In this thesis we calculate a set of evolutionary tracks of stars with 4 to 7 $M_{\odot}$ using the stellar evolution code Modules for Experiments in Stellar Astrophysics (MESA), varying the initial rotation rate and the metallicity. During the helium-burning phase, the luminosity increases as the rotation increases, while varying the metallicity the behavior of the luminosity is non-monotonic. On the other hand, the blue loop extension shows dependence on mass and rotation. The extension of the blue loop for stars with $M \leq 5.5\,M_{\odot}$ decreases as the rotation rate increases, while the behavior is non-monotonic for stars with $M > 5.5\,M_{\odot}$. Due to the loss of angular momentum during the H-shell burning phase, Cepheids do not reach near-critical rotations.

Using Radial Stellar Pulsations (RSP), the new functionality of MESA, we obtained the instability strip (IS) edges and linear periods for the fundamental mode. Period-age, period-age-temperature, period-luminosity, and period-luminosity-temperature relationships were obtained for three rotation rates and metallicities, they showed dependencies on crossing number, position in the IS, rotation, and metallicity. Period change rates (PCRs) were calculated directly from the linear periods. Models during the second crossing showed a non-monotonic dependence on rotation, while non-rotating tracks show a higher PCR during the third crossing. When varying the metal content, models with higher metallicity

present a slightly higher rate during the second crossing.

We compared our models with work presented in the literature using the Geneva code. We found large differences between the models given the different implementation of the rotation between codes. In addition, we compare our rates of period change with those calculated in recent work in the literature for Large Magellanic Cloud (LMC) Cepheids. We found good overall agreement, as 72.2% of the data fall within 3-sigma of the models. Implementations of physical processes not yet included in MESA, such as pulsation-driven mass loss, could help us to better cover the PCRs calculated in the literature.

Chapter 1

Introduction

Stellar lifetimes can reach billions of years, much longer than the 400-year life of modern astrophysics. Nevertheless, pulsating stars such as Cepheids or RR Lyrae offer us a window to measure and study changes due to stellar evolution. When these stars pulsate, their pulsation period depends on their average density. Evolutionary changes in the star's density will produce changes in the pulsation period, which will have a cumulative effect on the observed times of the star's maximum or minimum brightness. For this reason, among many others (see, e.g., Cox 1980; Catelan & Smith 2015; Neilson et al. 2016, and references therein), classical pulsators are laboratories for stellar astrophysics. Through the measurement of these period changes, together with theoretical models, we can test our understanding of stellar evolution.

1.1 Classical Cepheids

The first discovery of Cepheids was made by Edward Pigott who made naked-eye observations of η Aquilae variability in 1784, and a month later John Goodricke identified the variable δ Cephei, which became the prototype for the class of variables. At the turn of the twentieth century, Cepheids presented a problem for astronomers trying to understand the nature of their light changes. At that time, spectroscopic binary stars were discovered

(Vogel 1890). A few years later, Bélopolsky (1895) observed the spectrum of δ Cephei, finding that its radial velocity also changed during its light cycle. Bélopolski argued that Cepheid variability could be explained by eclipses in a binary star system. However, the light curves of Cepheids did not resemble the light curves of eclipsing binaries. These ideas remained until Shapley (1914) presented the argument that radial pulsation is responsible for the variations of Cepheid-type stars, although without detailing a model of how these pulsations occurred. He based his argument on the then recent discovery of the existence of giant and dwarf stars. Shapley argued that Cepheids were giant stars, so large that their radii exceeded the calculated sizes of the orbits in the supposed binary systems. A few years later, Eddington (1918, 1919) would be one of the first to discuss the physical processes that would be needed to keep a star pulsating. More than three decades later, Zhevakin (1953) and Cox & Whitney (1958) explained the specific driving mechanism behind the pulsations of Cepheid variable stars.

At present, our knowledge about classical Cepheids, also known as δ Cepheids, is much more extensive. They are evolved intermediate-mass stars of 2 to 20 $M_{\odot}$ (Turner 1996), that are located in a defined region in the Hertzsprung-Russell diagram (HRD) called the classic instability strip (IS). The theoretical evolutionary path of a 6 $M_{\odot}$ star that becomes a classical Cepheid is shown in Figure 1.1. Such a star pulsates as a Cepheid when it first crosses the IS as it evolves into the red giant branch, a phase called the Hertzsprung gap, where the star finishes core hydrogen burning and starts hydrogen-shell burning. Later, the star crosses the IS again during a blue loop, where the star fuses helium in its core. The evolutionary time scale of the first crossing is much faster than that of subsequent crossings, thus almost all observed Cepheids are considered to evolve along a blue loop and in the process of core helium burning.

Classical Cepheids are young stars, although they have already evolved beyond the main sequence, with ages ranging between 10^7 years for the massive and luminous Cepheids to 10^8 years for the faintest. For this reason, Classical Cepheids are only found in regions of recent star formation. In the Milky Way, they are found in the young disk population,

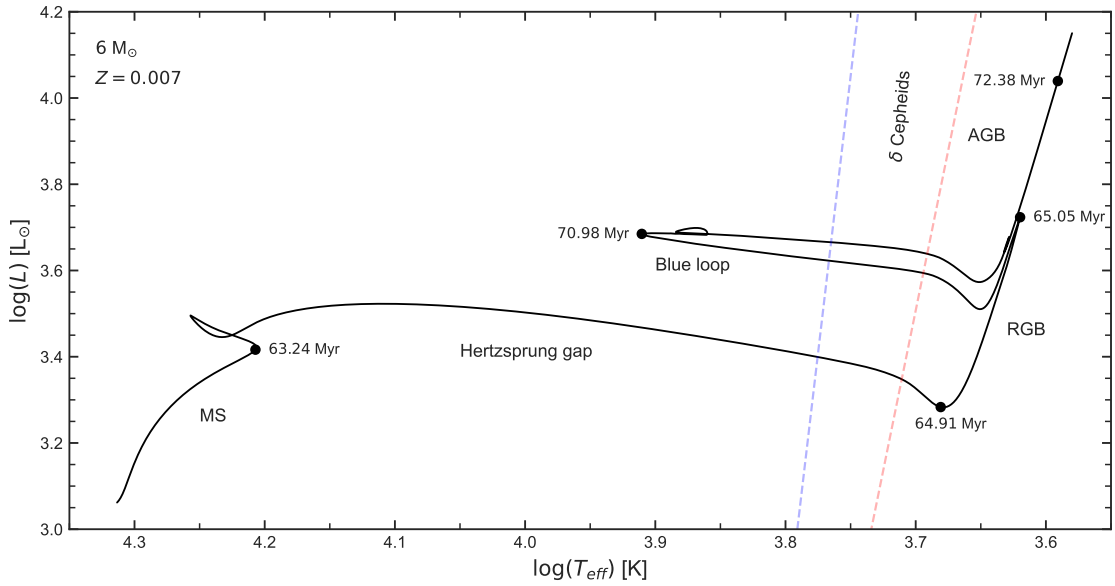

Figure 1.1: Evolution of an intermediate-mass star in the HRD. The evolutionary track shown was calculated with the code Modules for Experiments in Stellar Astrophysics (MESA) for $Z = 0.007$. The pre-MS and post-core-helium burning phases are omitted for clarity. After the MS, the amount of H in the core is insufficient to support the structure of the star through nuclear reactions, thus a rapid contraction occurs. The star then undergoes the phase of H-shell burning called Hertzsprung gap, with a convective envelope that begins to extend inward in mass and a rapidly expanding photosphere; at the base of the red-giant branch (RGB) occurs the first dredge-up, where processed material is brought to the surface; at the tip of the RGB He ignition occurs; the star goes through a loop during a core-He burning phase until He is exhausted, close to the base of the asymptotic giant branch (AGB). The boundaries of the classical IS, calculated with the functionality of MESA Radial Stellar Pulsations (RSP), are shown.

while they are also identified in nearby galaxies as the Andromeda Galaxy (M31) and the Magellanic Clouds (Catelan & Smith 2015). Cepheids obey a tight statistical relation between their pulsation period and luminosity (Leavitt 1908; Leavitt & Pickering 1912). For this reason, they are standard candles for determining distances to nearby galaxies, making them crucial objects in many determinations of the Hubble constant (e.g., Riess et al. 2019).

1.2 The κ and γ Mechanisms

In pulsation theory, to solve the non-adiabatic linear wave equation, a solution of the form (Catelan & Smith 2015):

$$\zeta(m,t) = \eta(m)e^{i\nu t}e^{-\kappa t} \tag{1.1}$$

is assumed, where η is the amplitude of the solution, $\nu = 2\pi/P$, and ν and κ are both real. In a quasi-adiabatic approximation , the stability coefficient for the mth pulsation mode is given by the following expression (Catelan & Smith 2015, and references therein):

$$\kappa_m = -\frac{\int_M (\delta T/T)_{m,\mathrm{ad}} \left(\delta\epsilon_{\mathrm{eff}} - \frac{\partial \delta L}{\partial m}\right)_m dm'}{2\nu_m^2 J_m}, \tag{1.2}$$

where J_m is the moment of inertia for adiabatic oscillations in the mth mode. The integral in the numerator of Equation 1.2 is called the *work integral* and represents, precisely, the total mechanical work that is transformed into kinetic energy of motion of the stellar layers during the pulsation cycle. The denominator term $\nu_m^2 J_m$ is proportional to the total pulsating kinetic energy of the star. Therefore, the absolute value of κ represents a timescale for the growth or damping of perturbations. When $\kappa < 0$, the instabilities grow over time and the star pulsates; on the other hand, if $\kappa > 0$, there is stability. Any regions of the star that contribute positively to the work integral are called *driving layers*, whereas those that contribute negatively are called *damping layers*.

To understand which are the layers of the star that contribute to the pulsation, let us assume, for simplicity, that the Rosseland mean opacity in a certain layer is roughly described by the Kramers (1923) opacity law, that is:

$$\kappa_R \propto \rho\, T^{-7/2}. \tag{1.3}$$

This expression indicates that, during compression, the Roselland mean opacity will be reduced due to the increase in temperature. However, it is possible to appreciate in Figure 1.2 that this is not true for the whole star. In the driving regions, we find ionized

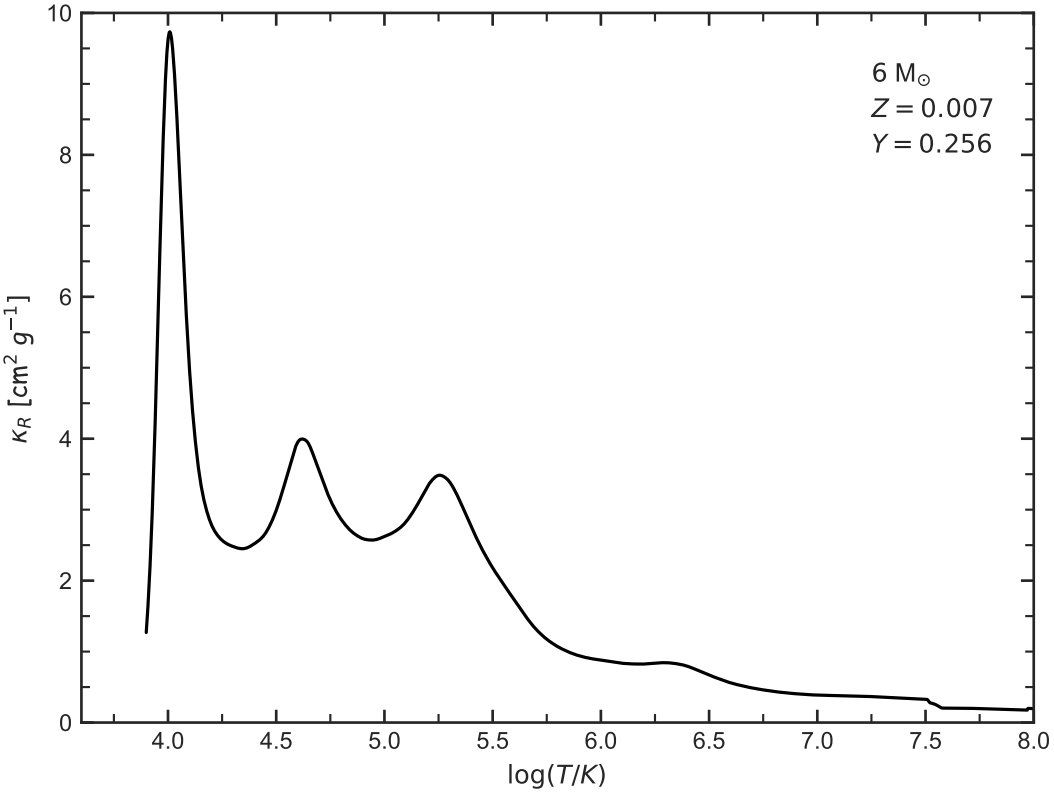

Figure 1.2: Rosseland mean opacity vs. temperature in a Cepheid model with 6 $M_\odot$, $Y = 0.256$ and $Z = 0.007$.

hydrogen and partially ionized helium. Most of the energy in these areas is used to ionize matter and not to heat it (Catelan & Smith 2015). If the Roselland mean opacity increases during compression, the consequence is that the corresponding region of the star will maintain the energy during compression, and will release it more easily during expansion acting as a driving layer. The increase in the Roselland mean opacity is referred to as the κ *mechanism*, and the increased ability of the same layer to gain heat during compression and release it during expansion is called the γ *mechanism*.

1.3 Period Changes

After the discovery of η Aquilae and δ Cephei, Chandler (1888) published one of the first catalogs of variable stars, followed by Nijland (1903), who suggested that the period of δ Cephei was changing over time. Chandler measured this change of period (Chandler 1896), obtaining -0.05 s yr^{-1}.

Eddington noted the importance of this measure and compared it with the stellar evolution theories of the time (Eddington 1919), finding that δ Cephei was evolving too slowly to generate energy from gravitational collapse. A century of observations of δ Cephei led Eddington to prove that there had to be another way of generating energy in the stars, building the foundation of modern stellar astrophysics.

By integrating the hydrostatic equilibrium equation under the constant density hypothesis, one can obtain an orders-of-magnitude expression that relates the period to the mean density:

$$\mathcal{P}\sqrt{\langle\rho\rangle} = \frac{\mathcal{P}\mathcal{M}^{1/2}}{\left(\frac{4}{3}\pi\right)^{1/2} R^{3/2}} = Q, \tag{1.4}$$

where $\mathcal{P}$ is the pulsation period, $\langle\rho\rangle$ is the mean density of the star, $\mathcal{M}$ is the stellar mass, R is the stellar radius, and Q is the pulsation constant. This expression is called *period-mean density relation*, and was first obtained by Ritter (1879). Recently, Turner et al. (2006, 2013) noted that Q is not strictly constant but has a small dependency on the period. Following their work, in which there assumed that there was no significant mass loss, the rate of change of the pulsation period $\dot{\mathcal{P}}$ can be expressed as

$$\frac{\dot{\mathcal{P}}}{\mathcal{P}} = \frac{5}{8}\left(\frac{\dot{L}}{L}\right) - \frac{5}{2}\left(\frac{\dot{T}_{\rm eff}}{T_{\rm eff}}\right). \tag{1.5}$$

Therefore, when a star evolves to brighter luminosities or cooler temperatures its period increases (first and third crossing of the IS), which implies that its rate of period change is positive. When the opposite occurs (second crossing of the IS), its period decreases, and its rate of period change is negative. This means that from the rate of change of the period one can know the evolutionary state of the star.

Over the last decades, there has been a large increase in the amount of data available of Cepheids. The current state of Cepheid period change measurements can be summarized in two cases: Cepheids in the Galaxy, and Cepheids in the Magellanic Clouds. The measurements in both the Small Magellanic Cloud (SMC) and the Large Magellanic Cloud (LMC) have been made mostly by the Massive Compact Halo Objects (MACHO) project (Alcock et al. 1996) and the Optical Gravitational Lensing Experiment (OGLE) survey (Paczynski et al. 1994); the latter is still ongoing. Soszyński et al. (2015) presented an almost complete census of classical Cepheids in the Magellanic Clouds consisting of 9535 Cepheids (4620 belong to the LMC and 4915 are members of the SMC). On the other hand, Soszyński et al. (2020) presented a collection of 1974 Galactic classical Cepheids. A new source of data is the project Digital Access to a Sky Century @ Harvard (DASCH; Grindlay et al. 2011) that aims to digitize the majority of the Astronomical Photographic Plate Collection and produce full photometry results for the entire sky.

With this enormous amount of data, studies have been conducted to compare these observational values of period change rates (PCRs) with those predicted by theory. Turner et al. (2006) used observations from DASCH and the American Association of Variable Star Observers (AAVSO) to measure period changes in nearly 200 Galactic Cepheids. They found that about two-thirds of Cepheids have positive PCRs whereas the remaining have negative rates, and these measurements were broadly consistent with the stellar evolutionary models of the time. Neilson et al. (2012) constructed state-of-the-art stellar evolution models of Cepheids that considered enhanced mass loss, and predicted results consistent with those of Turner et al. (2006). Anderson et al. (2014, 2016) calculated new stellar evolution models using the Geneva code that include rotation. They showed that rotation has a strong impact on the evolution of Cepheids and that including rotation in the models may be necessary to understand the measured PCRs. Recently, Miller et al. (2020) concluded that stellar rotation together with convective core overshooting are not sufficient to explain the observed distribution of PCRs, proposing pulsation-driven mass loss as the mechanism that should be additionally considered.

In this thesis, we use the version 15114 of the software Modules for Experiments in Stellar Astrophysics (MESA; Paxton et al. 2011, 2013, 2015, 2018, 2019), a state-of-the-art open-source 1D stellar evolution code, to compute a set of stellar evolutionary tracks of intermediate-mass stars, including rotation. With Radial Stellar Pulsation (RSP), the new functionality of MESA (Smolec & Moskalik 2008; Paxton et al. 2019), we obtained the PCRs in the three crossings of the IS for the calculated evolutionary tracks. We studied the effect of rotation on the rate of period change for these stars and compared the results with those obtained by Anderson et al. (2016). Rodríguez-Segovia et al. (in prep.) obtained PCRs for classical Cepheids in the LMC using DASCH, OGLE, and other datasets, and through a comparison with our results, we studied the evolutionary state of these stars.

The outline of this thesis is as follows: Chapter 2 describes the physics adopted in the MESA stellar evolutionary models, indicating the parameters used and the calibration performed; Chapter 3 describes the main features of the evolutionary models obtained, discussing certain implications and comparing them with models from other work; Chapter 4 presents the periods and PCRs obtained using the RSP functionality, in addition to presenting period-age and period-luminosity relationships, as well as a comparison with PCRs from other work. Finally, Chapter 5 presents our conclusions and future work.

Chapter 2

Adopted Physics

MESA has a unique modular structure that distinguishes it from most other stellar evolution codes. One of its main advantages is an easy and straightforward implementation of input physics or even new physics. The user input is given via the `inlist` file, which contains the user's choice for parameters for input physics, time step, mesh, and output options. The `run_star_extras.f` file allows the user to introduce new routines. In this section, we briefly review the relevant input physics adopted in the computed evolutionary models and their implementation in MESA.

2.1 Abundances

The determination of solar abundances has been a source of conflict between data observed by helioseismology and predictions made by models of the Sun's interior. Until 2005, it was considered that the solar metallicity was the one obtained by Anders & Grevesse (1989), which yielded models in good agreement with the speed of sound determined with helioseismology (Bahcall et al. 2005). However, Asplund et al. (2005) presented new solar abundances based on sophisticated 3D hydrodynamic models of the solar atmosphere, which led to a decrease in $Z_{\odot}$ and a worse agreement with helioseismological observations. This conflict is commonly known as the "solar abundance problem," and is still unsolved

(Bergemann & Serenelli 2014). Recently, Asplund et al. (2021) performed a recalculation of elemental abundances in the sun using highly realistic solar modeling and state-of-the-art spectroscopic analysis techniques. They found only a slight increase in the mass fraction of metals, keeping the solar abundance problem intact. The *protosolar* abundances $Y_{\odot}^{\rm ini}$ and $Z_{\odot}^{\rm ini}$, in addition to the abundance ratios of the other chemical species in the medium, of Grevesse & Sauval (1998) were adopted as the reference scale for all metallicities calculated in this work. The photospheric abundances vary over time, with respect to their protosolar abundance, as a consequence of diffusion, until they reach the current photospheric abundances of the Sun $Y_{\odot}^{\rm surf}$ and $Z_{\odot}^{\rm surf}$. The initial composition is set by assuming a linear enrichment law to the protosolar helium abundance as follows:

$$Y = Y_p + \left(\frac{Y_{\odot}^{\rm ini} - Y_p}{Z_{\odot}^{\rm ini}} \right) Z, \tag{2.1}$$

$$X = 1 - Y - Z, \tag{2.2}$$

where $Y_p = 0.2437$ is the primordial helium abundance (Planck Collaboration et al. 2020), $Y_{\odot}^{\rm ini} = 0.275$, $Z_{\odot}^{\rm ini} = 0.019$, and we adopted $Z = 0.005$, 0.007, and 0.009 as representative metallicities for LMC stars (Nidever et al. 2020).

2.2 Microphysics

2.2.1 Opacities

Ferguson et al. (2005) low-temperature tables and OPAL (Iglesias & Rogers 1993, 1996) high-temperature opacity tables are adopted. The OPAL tables are split into two types. Type I is used for $0.0 \leq X \leq 1.0 - Z$ and $0.0 \leq Z \leq 0.1$. Type II tables allow enhanced carbon and oxygen abundances, covering $0.0 \leq X \leq 0.7$ and $0.0 \leq Z \leq 0.1$. Type II opacities are particularly important for helium burning and advanced burning phases.

2.2.2 Equation of State

The equation-of-state (EOS) tables in MESA are based on the OPAL EOS tables (Rogers & Nayfonov 2002). At lower temperatures and densities there is a transition to the Saumon-Chabrier-Van Horn (SCVH) tables (Saumon et al. 1995). These extended MESA EOS tables cover $X = 0.0, 0.2, 0.4, 0.6, 0.8, 1$, and $Z = 0.0, 0.02, 0.04$. In addition, for temperature ranges and densities outside the range covered, the Helmholtz EOS (HELM, Timmes & Swesty 2000) and the Potekhin-Chabrier EOS (PC, Potekhin & Chabrier 2010) are used.

2.2.3 Nuclear Reaction Networks

We use nuclear reaction rates from the Nuclear Astrophysics Compilation of Reaction rates (NACRE, Angulo 1999). We adopted the `o18_and_ ne22.net` nuclear network in MESA. This nuclear network tracks and solves for the following species: ^{1}H, ^{3}He, ^{4}He, ^{12}C, ^{14}N, ^{16}O, ^{18}O, ^{20}Ne, ^{22}Ne and ^{24}Mg. This compact nuclear grid is suitable for our calculations, which include only the core hydrogen- and helium-burning evolutionary phases.

2.3 Macrophysics

2.3.1 Convection

Convective energy transport is commonly described by the mixing length theory (MLT), which has a free parameter $\alpha_{\rm MLT}$ that determines how far a fluid parcel travels before dissolving in the medium and depositing its energy. The location of convective regions is determined using the Ledoux criterion, which implies that a region is stable to convection if

$$\nabla < \nabla_{\rm L}, \tag{2.3}$$

where

$$\nabla_{\rm L} \equiv \nabla_{\rm ad} - \frac{\chi_\mu}{\chi_T}\nabla_\mu \tag{2.4}$$

and

$$\chi_\mu \equiv \left[\frac{\partial \ln P}{\partial \ln \mu}\right]_{\rho,T}, \tag{2.5}$$

$$\chi_T \equiv \left[\frac{\partial \ln P}{\partial \ln T}\right]_{\rho,\mu}. \tag{2.6}$$

In these expressions, ∇ is the material temperature gradient, $\nabla_{\rm ad}$ is the adiabatic temperature gradient and ∇_μ is the composition gradient. We adopt the version of MLT from Henyey et al. (1965), since it allows the convective efficiency to vary with the opaqueness of the convective element. This prescription requires two additional free parameters, ν and γ, which are multiplicative factors to the mixing length velocity and the temperature gradient in the convective element, respectively. We use a mixing length parameter of $\alpha_{\rm MLT} = 1.88$, that was constrained with a solar calibration (Subsection 2.3.8), and recommended default values of $\gamma = 1$ and $\nu = 8$ (Paxton et al. 2011). We consider a constant mixing length parameter, without taking into account dependencies on, for example, temperature and metallicity (Ludwig et al. 1999; Magic et al. 2015; Valle et al. 2019). Efforts are ongoing to eliminate this free parameter (e.g., Arnett et al. 2015; Pasetto et al. 2016). Convective mixing of elements is treated as a time-dependent diffusive process with a diffusion coefficient computed within the MLT formalism.

2.3.2 Convective Overshoot

In order to consider the nonzero momentum of a fluid element approaching the edge of the convective zone, defined by the Ledoux criterion, the convective region is extended beyond the edge thus defined. We adopted the exponential overshooting prescription implemented in MESA, in which the turbulent velocity field decays exponentially out of the convective boundary and eventually the convective elements disintegrate in the overshoot region through a diffusive process. According to the parameterization described

in Herwig (2000), the diffusion coefficient in the extended region is given by:

$$D_{\rm ov} = D_0 \exp\left(-\frac{2z}{f_{\rm ov} H_p}\right), \tag{2.7}$$

where $f_{\rm ov}$ is a free parameter that determines the efficiency of overshoot mixing, H_p is the local pressure scale height, and D_0 is the diffusion coefficient in the convectively unstable region at a depth $f_{0,\rm ov} H_p$ from the convective boundary. We adopt a value of $f_{\rm ov} = 0.019$, obtained by performing a solar calibration (Subsection 2.3.8). For simplicity, we consider that the efficiency of overshooting is the same for the core and the envelope, and $f_{0,\rm ov}$ is set to 0.5 $f_{\rm ov}$ as in Choi et al. (2016). In addition, more complex dependencies of this parameter were not considered. For instance, it has been suggested that the overshooting parameter is a function of mass and metal abundance (Woo & Demarque 2001; VandenBerg et al. 2006), although Claret (2007) showed that the dependence is less pronounced than was suggested by these authors. Recent efforts have been made to calibrate the overshooting parameter by means of two-dimensional hydrodynamic simulations (Higl et al. 2021).

2.3.3 Semi-Convection and Thermohaline Mixing

Semi-convection mixing occurs in regions that are unstable against convection according to the Schwarzchild criterion but stable according to the Ledoux criterion, thus

$$\nabla_{\rm ad} < \nabla < \nabla_{\rm L}. \tag{2.8}$$

The mixing in regions that satisfy Equation 2.8 is calculated by a time-dependent diffusive process. The diffusion coefficient is given by the following expression (Langer et al. 1983):

$$D_{\rm sc} = \alpha_{\rm sc} \left(\frac{K}{6 C_p \rho}\right) \frac{\nabla - \nabla_{\rm ad}}{\nabla_{\rm L} - \nabla}, \tag{2.9}$$

where $K = 4acT^3/(3\kappa_R \rho)$ is the radiative conductivity, C_p is the specific heat at constant pressure, and $\alpha_{\rm sc}$ is a dimensionless efficiency parameter. Semi-convection is important for stars with convective cores, as it can have a significant effect on the size of the core (Silva Aguirre et al. 2011; Paxton et al. 2013). Following Choi et al. (2016), we adopt $\alpha_{\rm sc} = 0.1$.

Similar to MLT theory, research is still being done to eliminate the free parameter of semi-convection (e.g., Wood et al. 2013).

Thermohaline mixing occurs in the presence of an inversion of the mean molecular weight in regions that are stable against convection according to the Ledoux criterion,

$$\nabla - \nabla_{\rm ad} \leq B \leq 0, \tag{2.10}$$

$$B \equiv -\frac{\chi_\mu}{\chi_T}\nabla_\mu. \tag{2.11}$$

In MESA, themohaline mixing is treated in a diffusive approximation, with a diffusion coefficient given by the analysis of Ulrich (1972) and Kippenhahn et al. (1980):

$$D_{\rm th} = \alpha_{\rm th}\frac{3K}{2\rho C_p}\frac{B}{(\nabla - \nabla_{\rm ad})}. \tag{2.12}$$

The parameter $\alpha_{\rm th}$ is a dimensionless efficiency that depends on the aspect ratio of the blobs or fingers arising from the instability. Themohaline mixing can occur due to the ^{3}He(^{3}He, 2p)^{4}He reaction, that takes place beyond the H-shell burning region during the red giant branch (RGB), horizontal branch (HB), and asymptotic giant branch (AGB) phases (Eggleton et al. 2006; Charbonnel & Zahn 2007). In the literature, proposed $\alpha_{\rm th}$ values covers two orders of magnitude (Kippenhahn et al. 1980; Charbonnel & Zahn 2007; Cantiello & Langer 2010). We adopt $\alpha_{\rm th} = 667$, since this value reproduces the surface abundances anomalies in RGB stars past the luminosity bump (Charbonnel & Zahn 2007).

2.3.4 Boundary Conditions

The pressure and temperature of the surface layers of a stellar model must be set by boundary conditions. These are set by model atmospheres calculated with the PHOENIX (Hauschildt et al. 1999a,b) and Castelli & Kurucz (2003) models. These boundary conditions are implemented in MESA in the `photosphere_tables` option, which cover $\log(Z/Z_\odot) = -4$ to +0.5, assuming the Grevesse & Noels (1993) solar abundance mixture, and they span $\log(g) = -0.5$ to 5.5 cm s^{-2} and $T_{\rm eff} = 2000 - 50000$ K. There is a small difference between the abundances of the boundary conditions with those adopted in the

stellar interior. Tests were performed by changing the abundances in the interior of our models to match those used in the boundary conditions. No significant differences were observed.

2.3.5 Diffusion

Diffusion and gravitational settlement of elements are essential in models of stellar evolution, causing modifications to the surface abundances and duration of the main sequence phase, as well as a shift in the evolutionary tracks to low luminosities and temperatures in the HRD, when diffusion is considered (Michaud et al. 1984; Salaris et al. 2000; Chaboyer et al. 2001; Stancliffe et al. 2016). MESA performs diffusion and gravitational settlement calculations following the method of Thoul et al. (1994). The elements present in the stellar model are categorized into five "classes" according to their atomic mass, each of which has a representative element whose properties are used to calculate the diffusion velocities. We adopt the default set of MESA for representative members; these are ^{1}H, ^{3}He, ^{4}He, ^{16}O, and ^{56}Fe. Atomic diffusion coefficients are calculated following Paquette et al. (1986). Then, the diffusion equation is solved using the total mass fraction within each class.

2.3.6 Rotation

The rotation of stars has been widely studied from an evolutionary perspective (e.g., Pinsonneault et al. 1990; Maeder & Meynet 2000; Heger & Langer 2000; Ekström et al. 2012; Georgy et al. 2013), but its effects on models of stellar evolution remain an uncertain problem. Stellar structure deviates from spherical symmetry in the presence of rotation. While the structure is inherently 3D, it is possible to solve the stellar structure equations in one dimension by assuming the "shellular approximation" (Kippenhahn & Thomas 1970; Meynet & Maeder 1997; Paxton et al. 2013). This approach is valid if the angular velocity is constant over isobars, which is to be expected in the presence of strong anisotropic

turbulence acting on these isobars due to differential rotation (Zahn 1992).

In MESA, modifications to the stellar structure equations are made by introducing two correction factors, namely f_P and f_T, to the momentum balance and the radiative temperature gradient (see Paxton et al. 2013, 2019). Previous versions of MESA used Endal & Sofia (1976) method, which considers deviations of the Roche potential from the spherically symmetric, to calculate f_P and f_T. These parameters need a minimum value to ensure numerical stability ($f_P = 0.75$ and $f_T = 0.95$). Paxton et al. (2019) implemented analytical fits to the Roche potential, that do not need to establish a minimum for f_P and f_T, in order to improve the calculations of models with high rotation. However, after numerous tests carried out in this work, numerical stability was not achieved for models with $\omega > 0.5$ using these analytical fits. Therefore, the minimum values of f_p and f_T were adopted, which correspond to a maximum rotation rate of 60% of the critical rotation. Results for high rotation models should accordingly be treated with caution, since corrections to the structure equations may be underestimating the effects of rotation.

Initial rotation is defined in the zero age main sequence (ZAMS) as solid-body rotation. The input parameter for varying the rotation rate is the ratio of the initial surface angular frequency to the critical angular frequency $\omega_0 = \Omega_{\rm ZAMS}/\Omega_{\rm crit}$. The critical angular frequency is defined as

$$\Omega_{\rm crit} = \sqrt{GM/R_{\rm eq}^3}, \tag{2.13}$$

where $R_{\rm eq}$ is the equatorial radius when the star reaches critical rotation. In this work we calculate stellar evolution models with $\omega_0 = 0.1, 0.2, 0.3, 0.4, 0.5, 0.6, 0.7, 0.8, 0.9$. We stress that the results for $\omega_0 > 0.6$ should be treated with caution, due to the minimum values adopted for correction parameters due to rotation.

The transport of angular momentum and chemical elements due to rotation-induced instabilities is implemented in MESA in a diffusive approach, as described in Endal & Sofia (1978). It is important to note that other codes of stellar evolution, such as Geneva (Eggenberger et al. 2008) and RoSE (Potter et al. 2012), implement a diffusion-advective description (Zahn 1992), different from that of MESA. These two approaches are

equivalent for the transport of elements but can cause great differences in the transport of angular momentum. MESA calculates diffusion coefficients for five rotationally induced mixing processes: dynamical shear instability, Solberg-Høiland instability, secular shear instability, Eddington-Sweet circulation, and the Goldreich-Schubert-Fricke instability. A detailed description of the physics of these phenomena and the calculation of the respective diffusion coefficients can be found in Heger et al. (2000). This diffusive implementation of transport of angular momentum and chemical elements has two free parameters, namely f_c, which represents the ratio of the diffusion coefficient to the turbulent viscosity and scales the efficiency of composition mixing to that of angular momentum transport, and f_μ, which relates the sensitivity of the rotational mixing to the mean molecular weight gradient. In other words, a small f_c corresponds to a process that transports angular momentum more efficiently than it can mix material, and a small f_μ means that the rotational mixing is efficient even in the presence of a stabilizing ∇_μ. We consider $f_c = 1/30$ and $f_\mu = 0.05$ after Choi et al. (2016), who demonstrate that these values produce surface nitrogen enhancements that are in reasonable agreement with the observations.

2.3.7 Mass loss

Mass loss is treated with the Reimers (1975) prescription for the RGB. This scheme depends on global stellar properties as follows:

$$\dot{M}_{\rm R} = 4 \times 10^{-13} \eta_R \frac{(L/L_\odot)(R/R_\odot)}{(M/M_\odot)} M_\odot \ {\rm yr}^{-1}, \tag{2.14}$$

where η_R is a scaling factor of order unity. As in Anderson et al. (2016), we adopt a value of $\eta_{\rm R} = 0.5$ for stars of 4 and 5 $M_\odot$, and $\eta_{\rm R} = 0.6$ for stars of 6 and 7 $M_\odot$. Since our models do evolve up the AGB, for completeness we state also that we consider a minor loss of mass in the AGB given by the scheme of Blöcker (1995),

$$\dot{M}_{\rm B} = 4.83 \times 10^{-9} \eta_{\rm B} \frac{(L/L_\odot)^{2.7}}{(M/M_\odot)^{2.1}} \frac{\dot{M}_{\rm R}}{\eta_{\rm R}} M_\odot \ {\rm yr}^{-1}, \tag{2.15}$$

where $\eta_{\rm B} = 0.0003$. Since our interest lies in the stages prior to the AGB, this assumption does not affect any of our results.

In addition to the above prescriptions, MESA includes rotation-enhanced mass loss as a function of the surface angular frequency Ω as follows:

$$\dot{M}(\Omega) = \dot{M}(0)\left(\frac{1}{1-\Omega/\Omega_{\rm crit}}\right)^{\xi}, \tag{2.16}$$

where $\dot{M}(0)$ is the standard mass-loss rate (Reimers or Blöcker) and we adopt $\xi = 0.43$ (Langer 1998). Some of our models reached critical rotation during their evolution; in such cases, we expect a strong increase in mass loss in the equatorial region. The exact details of this process are still unknown and require simulations that combine hydrodynamics and radiative transfer. In response to this situation, MESA implements a "mechanical mass loss," which removes the super-critical layers and keeps the surface below the critical velocity.

2.3.8 Solar Calibration

Parameter	Target	Model value	Fractional error (%)
$L_\odot$ (10^{33} erg s^{-1})	3.828^a	3.823	0.13
$R_\odot$ (10^{10} cm)	6.957^a	6.957	0.005
$T_{\rm eff,\odot}$ (K)	5772^a	5774	0.03
$Y_\odot^{\rm surf}$	0.2485^b	0.2503	0.72
$Z_\odot^{\rm surf}/X_\odot^{\rm surf}$	0.0231^c	0.0248	7.36
$R_{\rm cz}$	0.713^b	0.717	0.56
$\alpha_{\rm MLT}$	...	1.88	...
$f_{\rm ov}$	...	0.019	...

Table 2.1: Solar calibration results. ^{a} Mamajek et al. (2015), ^{b} Basu & Antia (2004), ^{c} Grevesse & Sauval (1998).

As mentioned in the previous sections, a calibration of the mixing length parameter and the overshooting parameter was performed using the constraint of the location of the base of

the convective zone $R_{\rm cz}$ obtained using helioseismic data (Basu & Antia 2004) and surface properties of the Sun (Mamajek et al. 2015). We used the `simplex_solar_calibration` test suite, which uses the simplex optimization algorithm (Nelder & Mead 1965) to find models that minimize a specific χ^2 to obtain a set of parameters that reproduce observationally inferred solar parameters. For each iteration, a new choice of the mixing length parameter and the overshooting parameter is set and the model is evolved from the pre-MS to 4.61 Gyr. A χ^2 value is computed by summing over the $\log L$, $\log R$, $T_{\rm eff}$, surface composition, and $R_{\rm cz}$ with user-defined weights. This process is repeated until the tolerance parameters are met.

The results of the solar calibration are shown in Table 2.1. Although many initial assumptions and variations of diffusive parameters were explored, we did not obtain a model that satisfies all available solar observations. In particular, the largest discrepancies are found in the ratio of surface abundances $Z_{\odot}^{\rm surf}/X_{\odot}^{\rm surf}$, which is different from that obtained in the calibration performed by Choi et al. (2016) using the Asplund et al. (2009) abundances, where they obtain the largest discrepancies in the surface helium abundance.

We accordingly adopt a solar-calibrated $\alpha_{\rm MLT} = 1.88$ for all masses and an overshoot parameter for the envelope and the core $f_{\rm ov,\,env} = f_{\rm ov,core} = 0.019$ ($f_{0,\rm ov,\,env} = f_{0,\rm ov,\,core} = 0.5 f_{\rm ov,\,env}$).

Chapter 3

Stellar Evolution Models

We calculate evolutionary tracks that cover stellar masses from 4 to 7 $M_\odot$, uniformly spaced in mass with steps of $0.5\,M_\odot$, metallicities of $Z = 0.005$, 0.007, and 0.009, helium abundances of $Y = 0.256$, 0.259 0.252, respectively, and a rotation rate range of $\omega_0 \equiv \Omega_{\rm ZAMS}/\Omega_{\rm crit}$ from 0.0 to 0.9. The evolution is calculated from the pre-MS stage to a limit in luminosity that allows the thermal-pulse AGB phase to be avoided. The latter was considered since post-AGB phases are computationally expensive and are not relevant to our study of classical Cepheids.

3.1 Basic Properties of the Models

3.1.1 HRD

Figure 3.1 shows the calculated evolutionary tracks with $Z = 0.007$. Tracks with metallicities $Z = 0.005$ and $Z = 0.009$ are shown in Figure 3.2. The temperature of the ZAMS becomes progressively lower as the rotation rate increases, reaching temperature differences of up to $\sim$ 1700 K. In rotating models, this initial evolutionary phase is dominated by the centrifugal force (Meynet & Maeder 2000), which decreases the effective gravity acceleration $g_{\rm eff}$. Since $T_{\rm eff} \propto g_{\rm eff}^{1/4}$, in a rotating star at the ZAMS the effective

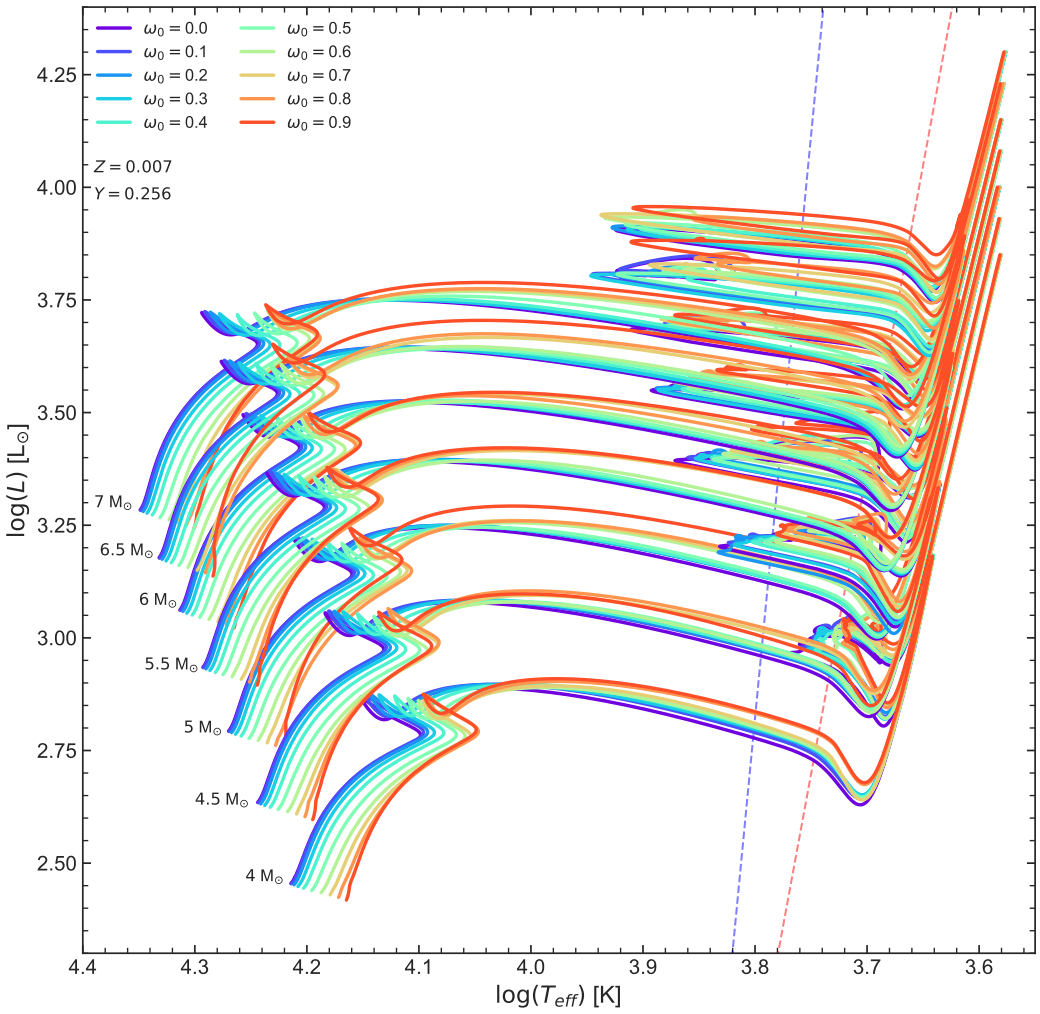

Figure 3.1: HRD of the evolutionary tracks computed with MESA, assuming a metallicity of $Z = 0.007$ and a helium abundance of $Y = 0.256$. Lines of different colors correspond to different ω_0, following the color scheme given at the top left of the panel. Averaged IS boundaries of fundamental radial pulsation calculated with RSP, are plotted. Pre-main-sequence evolution is omitted for clarity.

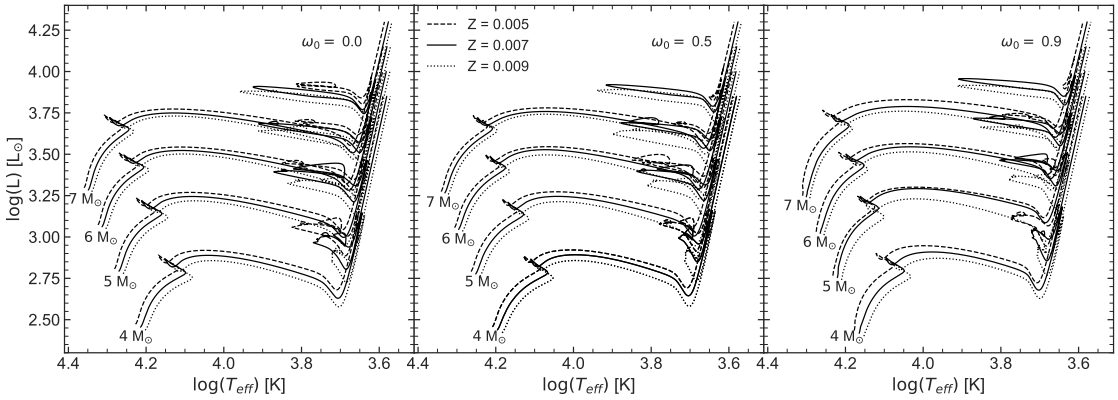

Figure 3.2: HRD showing the computed evolutionary tracks, assuming $\omega_0 = 0.0$ (left panel), 0.5 (middle panel), and 0.9 (right panel). In each case, tracks are shown for masses, from bottom to top, of 4, 5, 6, and 7 $M_\odot$, respectively. Results for three different metallicities are also displayed in each panel, namely $Z = 0.005$ (dashed lines), 0.007 (solid lines) and 0.009 (dotted lines).

temperature is expected to be lower (von Zeipel 1924). During the MS, the behavior of the luminosity as a function of rotation is related to the mass of the convective core, which is affected by a competition between two physical effects. On one hand, the centrifugal force generates additional support to gravity, which tends to decrease the size of the core and its luminosity. On the other hand, the opposite occurs due to rotational mixing, which brings hydrogen-rich material to the convective core, slowing down its decrease in mass and extending the duration of the MS, as shown in Figure 3.3, leading to an extension of its duration of 15.4% on average. In addition, rotational mixing transports helium and nitrogen to the radiative envelope. This material decreases the opacity of that medium, which produces an increase in the luminosity.

At the same stellar age, a non-rotating model is brighter than a rotating one, indicating that the centrifugal force is more effective at decreasing the core size than is rotational mixing at increasing it. The behavior of the luminosity is opposite to the one previously mentioned during the phase of H-shell burning, since we notice that, as the rotation rate increases, the evolutionary tracks become more luminous.

A closer view of the evolution of the models during the blue loop is shown in Figure 3.4.

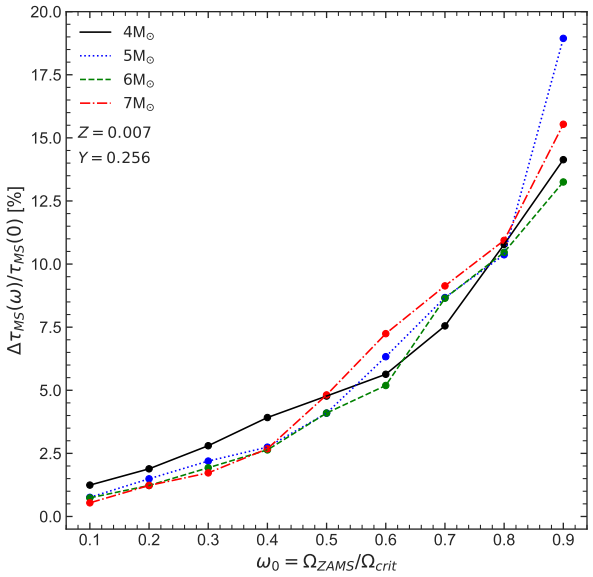

Figure 3.3: MS duration enhancement, computed for models with metallicity $Z = 0.007$ and helium abundance $Y = 0.256$, as a function of the initial rotation rate parameter ω_0. Lines of different colors and styles correspond to different masses, namely 4 (black solid line), 5 (blue dotted line), 6 (green dashed line), and 7 $M_\odot$ (red dashed-dotted line).

These loops are the consequence of an excess of helium above the H-burning shell, which results from the contraction of the convective core during core hydrogen burning. The outward movement of the burning shell removes the excess helium and produces the loop (Walmswell et al. 2015). Blue loops are very sensitive to input physics, such as convective core overshooting, metallicity, and nuclear reactions (Xu & Li 2004a,b; Walmswell et al. 2015). In general, we notice that there is an increase in the luminosity of the loops as the rotation rate increases. For $M \leq 5.5\,M_\odot$, the blue loop extension decreases as the rotation rate increases. However, this does not occur in tracks with $M > 5.5\,M_\odot$, where the loop extension behavior is non-monotonic. A similar phenomenon can be observed in the models presented in Georgy et al. (2013).

We note that some models, especially the $4 - 5$ $M_\odot$ tracks, exhibit multiple loops during the He-burning phase. These are commonly called "He-spikes", which in some cases produce a fourth and even fifth crossing of the IS. An example of this phenomenon

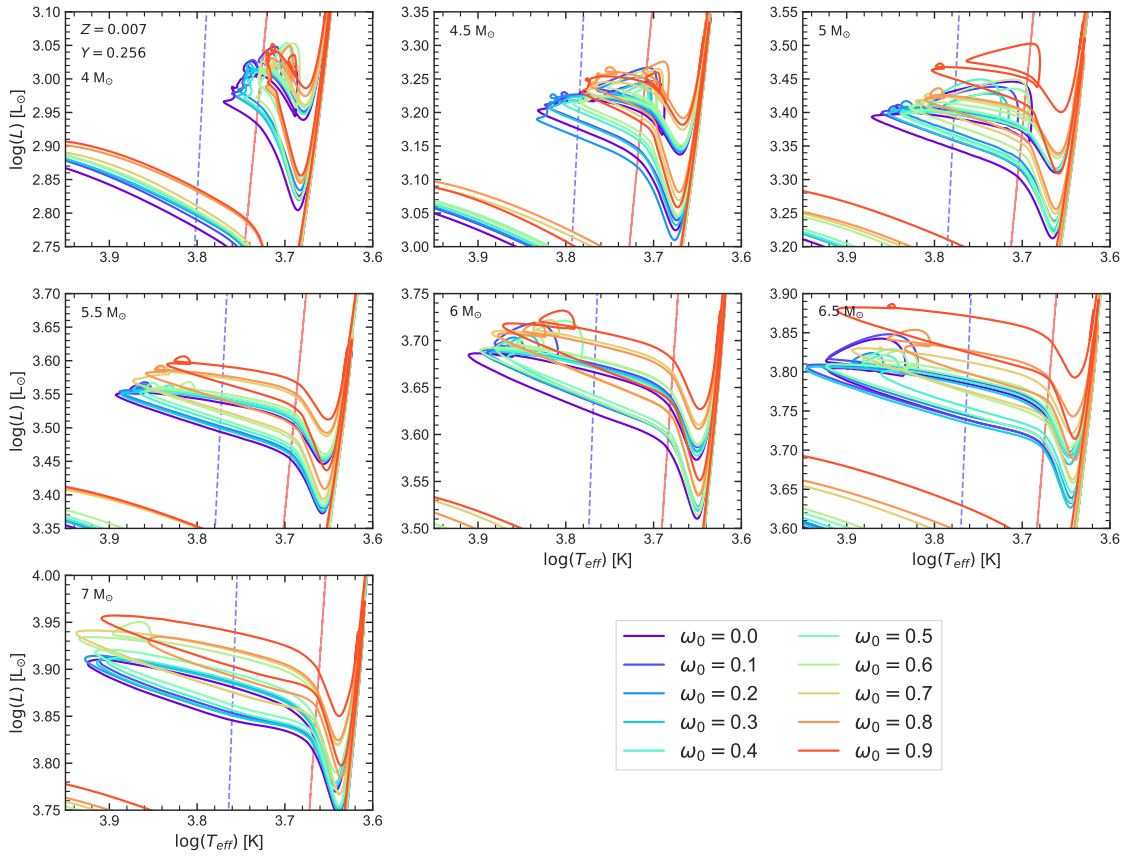

Figure 3.4: Evolution in the HRD of models with metallicity $Z = 0.007$ and helium abundance $Y = 0.256$ during core-He burning. Red and blue averaged IS boundaries for fundamental-mode pulsation, computed using RSP, are overplotted. From upper left to bottom left, results are shown for masses from 4 to 7 $M_\odot$ in steps of 0.5 $M_\odot$, with mass values increasing to the right along each row. Lines of different colors correspond to different ω_0, following the color scheme given at the bottom right of the figure.

can be seen in Figure 3.5, where the non-rotating evolutionary track for a 4 $M_\odot$ star is plotted on the left panel and the central abundance of helium on the right panel, and three colored marks were added to the curves indicating three consecutive moments in time when the central He abundance presents sudden increases. The existence of the loops present in the track is directly associated with sudden increases in central helium abundance. It is unlikely that these He-spikes are real, although small mixing events within

a semiconvective zone at the edge of the convective core that move a small amount of helium inwards (Sweigart & Renzini 1979), could produce a similar effect. In MESA, they are associated with the uncertainty of the location of the edge of the convective core, and the mixing that occurs at this interface. A small displacement of this boundary can mix a significant amount of helium in the core, which produces an increase in energy generation. This ends up producing noticeable changes in the luminosity of the star. The main effect of these He-spikes is the alteration of the lifetimes for the third crossing, which can produce discrepancies in the predictions for the ratio of asymptotic giant branch to horizontal branch stars in globular clusters (Constantino et al. 2017). Recently, the version of MESA used in this work implemented a new approach for the treatment of convective boundaries called "convective premixing (CPM)" scheme (Paxton et al. 2019). The CPM scheme is applied at the start of each time step, before any structural or compositional changes due to stellar evolution. It finds the boundary cells between the convective and radiative zones, and considers whether the radiative face of the cell would change if the adjacent cell outside the convective region is completely mixed with the rest of the convective region. If the radiative face of the boundary cell becomes convective during this putative mixing, the mixing is applied in the model. This process continues iteratively until the radiative face of the current convective boundary remains radiative during the putative mixing. Although this scheme is an improvement, the correct treatment of the convective edge continues to be a challenging problem.

Small changes in Z lead to significant changes in temperature and luminosity in the HRD. During core- and shell-hydrogen burning, the decrease in metal content makes the evolutionary track hotter and more luminous due to a lower Rosseland mean opacity. During core-He burning, differences in stellar envelope opacity play an important role in the behavior of the blue loops. Walmswell et al. (2015) concluded that the higher the metallicity the less pronounced the blue loop becomes, as a general trend. However, the sensitivity of loop extension to the input physics adds a higher degree of complexity. In Figure 3.2 we observe how the general trend holds for stars of 4 solar masses, but the

behavior for more massive stars is more intricate, with the blue loop being completely suppressed for stars with 7 solar masses and $Z = 0.005$. There are a number of important ingredients that determine whether a star develops a blue loop or not. Among those, the ratio of the envelope convection mass to the total envelope mass at the bottom of the RGB is essential. Stellar models with very low or high metallicity are found to develop blue loops when this ratio is lower than a critical value between 0.3 and 0.45 (Xu & Li 2004a,b). In addition, the latter may depend on other physical parameters such as mass loss, overshooting, diffusion, etc. Therefore, it is expected to find a non-monotonic behavior when studying the extension of blue loops, and we will not explore it in detail in this work.

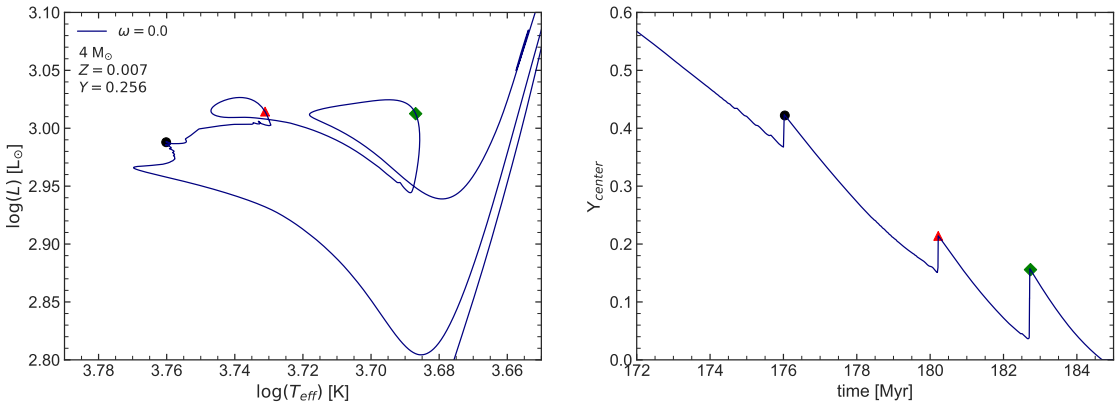

Figure 3.5: Example of the "He-spikes" phenomenon. In the left panel an HRD of a non-rotating evolutionary track of a $4\,M_\odot$ star, in the right panel the central helium abundance as a function of time. Three colored dots in both panels indicate three simultaneous moments in time.

3.1.2 Evolution of the Mass of the Convective Core

As mentioned above, the centrifugal force produces an additional support against gravity, which decreases the size of the convective core and the temperature of the star in the ZAMS. After this phase, the greater the efficiency of the mixing produced by rotation, the larger the core becomes. This behavior can be observed in Figure 3.6. We can notice that, for models with high rotation, the decrease in size of the core is less steep just after

the ZAMS. This effect is particularly significant for $5\,M_{\odot}$ tracks, where the mass of the convective core for the rotation rate of $\omega_0 = 0.9$ is notably higher than the others.

During the evolution in the MS, numerical instabilities are sometimes found, mainly in evolutionary tracks of $4\,M_{\odot}$. These fluctuations are associated to uncertainties in the location of the convective boundary. Nevertheless the mass of the convective core recovers its general trend in a short time scale, and thus these instabilities do not affect the later evolution of the stars. After the exhaustion of the central H, the core stops being convective during the H-shell burning resulting in an abrupt decrease in the mass of the convective core. At the base of the RGB, the core begins to grow again, until the hottest point of the blue loop. During this phase, small variations of the mass of the convective core are observed, associated with mixing episodes that produce small bumps in the luminosity, which can be seen in Figure 3.4, near the second crossing of the IS. After the hottest point of the blue loop, the core starts to shrink again, but a slight increase is observed in some tracks. This can be seen in the zoom in the upper and lower left panels of Figure 3.6. This increase is associated with the He-spikes, as mentioned above.

3.1.3 Evolution of the Surface Angular Frequency of Rotation

The evolution of the surface rotational angular frequency is shown in Figures 3.7 and 3.8. Three physical processes are responsible for the evolution of the rotation rate: conservation of angular momentum, which modifies ω when the star contracts or expands; internal transport mechanisms (Endal & Sofia 1978), which redistribute the angular momentum along the stellar interior; and mass loss, which removes angular momentum from the surface.

During the MS, the Eddington circulation is one of the most important mechanisms to change the angular momentum distribution (Endal & Sofia 1978), as it carries angular momentum from the inner parts to the surface, accelerating the latter. On the other hand, mass loss increased by rotation removes angular momentum (Langer 1998). In Figure 3.7, we notice how ω stably increases during the MS, with the exception of the tracks with

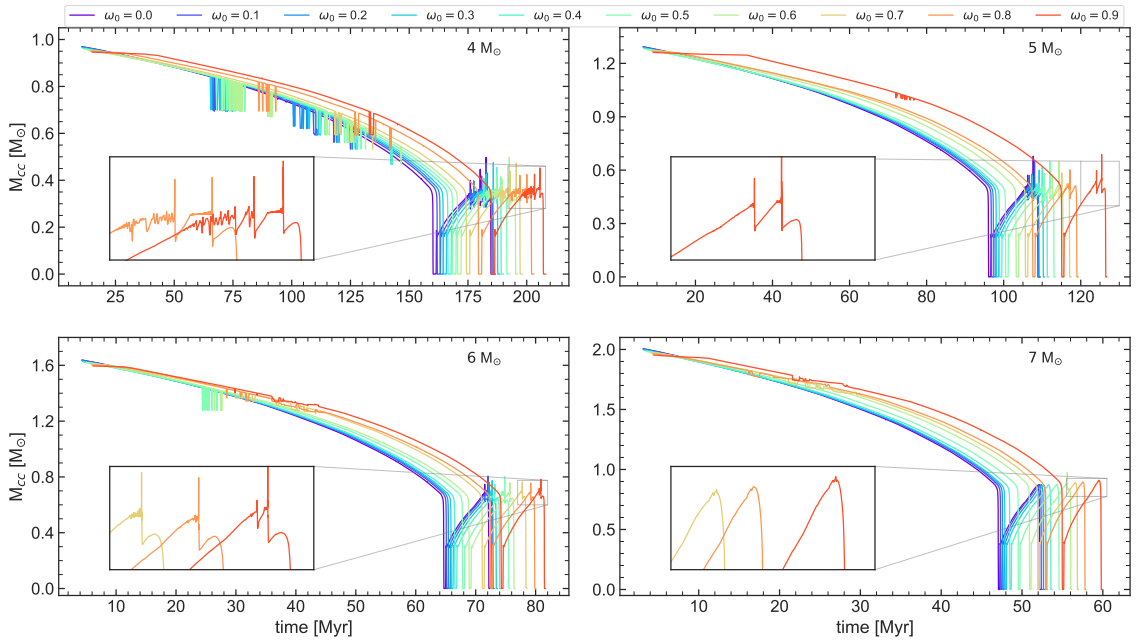

Figure 3.6: Evolution of the mass of the convective core for 4 (upper left), 5 (upper right), 6 (bottom left), and 7 $M_\odot$ (bottom right). The mass of the convective core at the bluest point of the blue loop is shown in each zoomed-in panel. In each panel, lines of different colors correspond to different ω_0, following the color scheme given at the top of this figure.

$\omega_0 \geq 0.8$, where at the end of the MS a small decrease in ω is observed. At these high rotation rates, the increased mass loss due to rotation becomes considerable, decreasing the rotation rate by removing angular momentum.

After the exhaustion of the central hydrogen, an overall contraction of the star occurs, which considerably increases ω. For models with high rotation rates, this contraction increases the surface angular frequency to the critical frequency, as can be seen in Figure 3.8. When this occurs, the mechanical mass loss mechanism is activated, keeping the surface below the critical frequency limit by removing the outermost layers. During the H-shell burning phase, the rapid expansion of the star envelope dramatically decreases ω. During He-burning, ω increases again until the bluest part of the blue loop, then decreases as the star evolves towards the AGB. We note that, for $\omega_0 \leq 0.7$, ω becomes comparable to or even larger than ω_0 during helium burning. On the other hand, for $\omega_0 > 0.7$, the

maximum magnitude of the surface rotational angular frequency is always smaller than ω_0 and remains constant for all masses, which is related to the conservation of angular momentum during this evolutionary phase. A slight increase in ω is observed in stars with He-spikes, similar to the behavior of the convective core mass. It follows from Figure 3.8 that it would not be possible to observe a Cepheid with a near-critical rotation rate in this mass range due to the loss of angular momentum during the H-shell burning phase, in addition to the enhanced mass loss by rotation during the helium-burning phase.

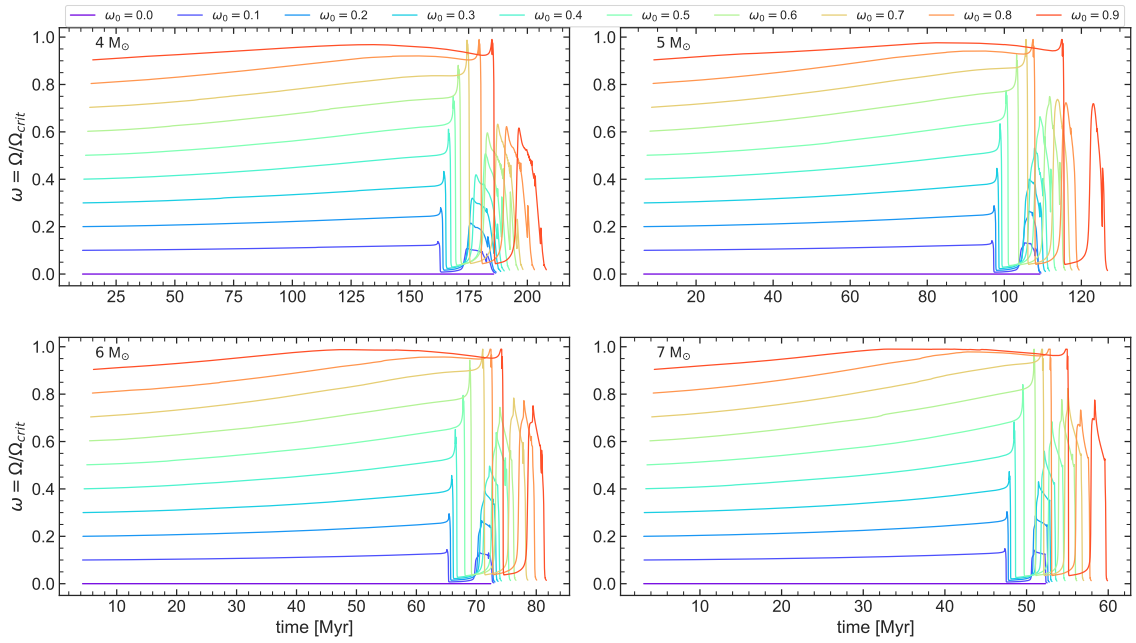

Figure 3.7: Evolution of the surface angular frequency of rotation for 4 (upper left), 5 (upper right), 6 (bottom left), and 7 $M_\odot$ (bottom right). In each panel, lines of different colors correspond to different ω_0, following the color scheme given at the top of this figure.

3.2 Comparison with Anderson et al. (2016)

Anderson et al. (2016) present the first detailed pulsational instability analysis of stellar evolution models that include rotation, for fundamental mode and first overtone classical Cepheids alike. They use the Geneva code of stellar evolution (Eggenberger et al. 2008),

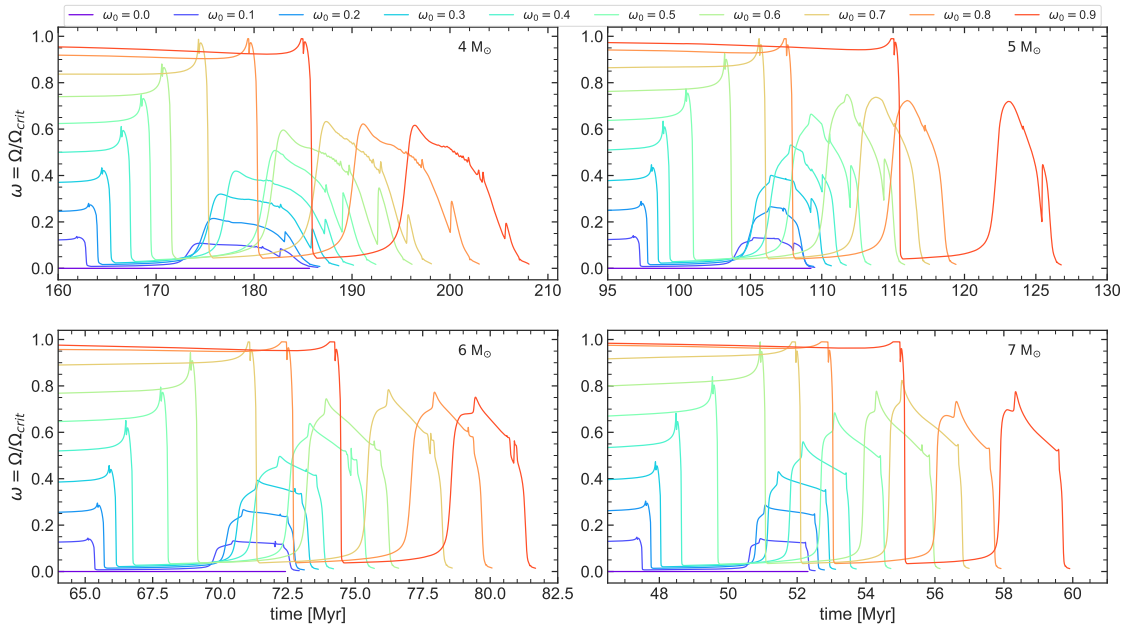

Figure 3.8: Close up of evolution of the surface angular frequency of rotation for 4 (upper left), 5 (upper right), 6 (bottom left), and 7 $M_\odot$ (bottom right). In each panel, lines of different colors correspond to different ω_0, following the color scheme given at the top of this figure.

varying mass, metallicity, and rate of rotation. Since the pulsation analysis presented in Anderson et al. (2016) was performed for metallicities of $Z = 0.014$, 0.006 and 0.002, we used the interpolation interface provided by the Synthetic Clusters Isochrones & Stellar Tracks (SYCLIST) web portal, available at `https://www.unige.ch/sciences/astro/evolution/en/database/syclist/`. This web resource performs an interpolation on the grid of stellar models presented in Georgy et al. (2013), in order to obtain evolutionary tracks with masses of 5 and 7 $M_\odot$, metallicity of $Z = 0.007$, and rotation rates of $\omega_0 = 0.0$, 0.5, and 0.9.

A plot comparing the evolutionary tracks of 5 and 7 $M_\odot$ obtained in this thesis and in Anderson et al. (2016) in an HRD is shown in Figure 3.9. We noticed major differences between models, such as in the position of the ZAMS, the extension of the MS, the H-shell burning phase, the position of the RGB, and the behavior of the blue loop. Some of these differences can be explained by the different parameters adopted, in particular the

mixing length and the overshooting parameter. Anderson et al. (2016) uses Georgy et al. (2013) models, which adopted a mixing length of $\alpha_{\rm MLT} = 1.65$ and an implementation of instantaneous overshooting with a parameter of $f_{\rm ov} = 0.1$. It is important to mention that neither of these parameters was calibrated in their work, whereas our models are properly calibrated to the Sun. In addition, the temporal resolution of the models calculated in this work is much higher than the resolution of the models of Anderson et al. (2016): the time step of the models calculated with MESA is between 1 to 4 orders of magnitude lower than the time step used to compute the models presented in Anderson et al. (2016).

We created a non-rotating evolutionary model with MESA adopting the same mixing length and overshooting parameters as in Anderson et al. (2016). An HRD comparing our track with theirs is shown in Figure 3.10. We notice that the tracks are very similar, with the exception of the behavior in the blue loop, where the track calculated with MESA presents a He-spike, due to the different treatment of the convective boundary. However, matching these parameters was not enough to eliminate the differences between our rotating models and those from Anderson et al. (2016). This is related to the different implementations of rotation in the Geneva and MESA codes, as mentioned in Section 2.3.6.

A sample of these different implementations can be seen in Figure 3.11, where the evolution of the rotation rate is shown. A sudden decrease of ω is observed in the models of Anderson et al. (2016), this corresponds to the time that the model reaches a state of quasi-equilibrium, since their initial profile of ω is assumed as solid-body rotation which is readjusted to differential rotation. In our models, this does not occur since the rotation rate is set near the ZAMS, and its value relaxes over a number of steps until the desired value is reached. The evolution of ω during the helium-burning phase is significantly different between models. We note that ω in the most blueward point of the blue loop is higher in our models, thus our evolutionary tracks produce helium-burning stars with higher rotation rates than those predicted by the models from Anderson et al. (2016). To confirm the existence of these stars, it is necessary to study the distribution of rotation rates in LMC, which is beyond the scope of this work. The behavior of the blue loop of the

models with the Geneva code becomes spectacular for $\omega_0 = 0.9$, covering a much greater range in luminosity than our models. These differences can result in discrepancies in the calculated values for the PCRs, which were compared in section 4.4.

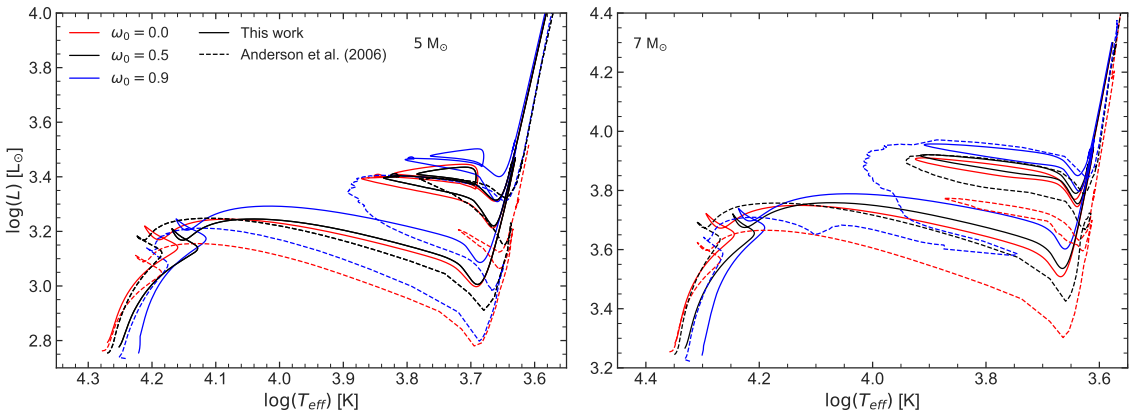

Figure 3.9: HRD comparing evolutionary tracks of this work (solid lines) with tracks from Anderson et al. (2016) (dashed line). Left panel shows 5 $M_\odot$ tracks, while right panel shows 7 $M_\odot$ tracks. In each panel, lines of different colors correspond to different ω_0, namely $\omega_0 = 0$ (red), $\omega_0 = 0.5$ (black) and $\omega_0 = 0.9$ (blue).

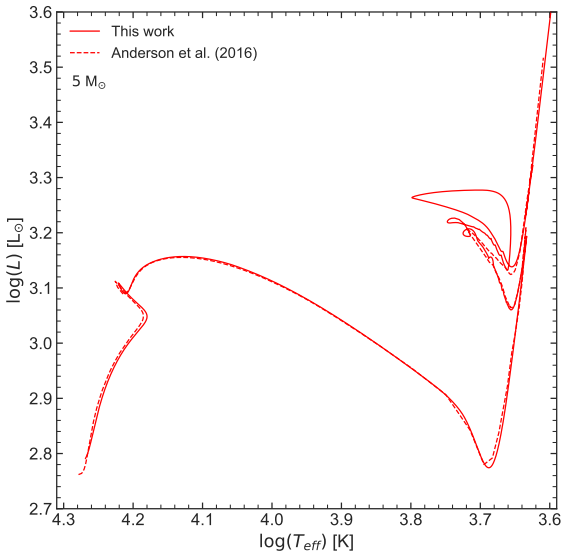

Figure 3.10: HR diagram comparing a non-rotating track of 5 $M_{\odot}$ from this work (solid lines) with a track from Anderson et al. (2016) with the same mass and chemical composition (dashed line). The same parameters were adopted for the mixing length and the instantaneous overshooting parameter to match Anderson's evolutionary track.

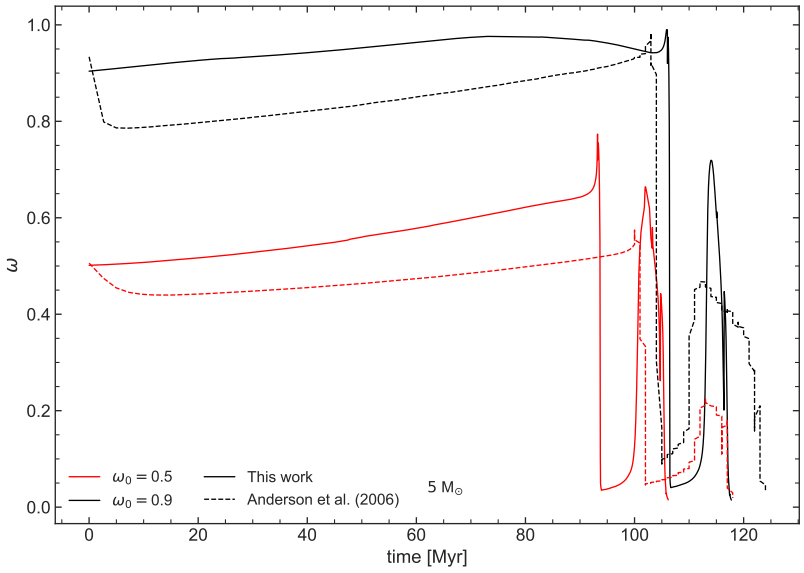

Figure 3.11: Comparison of the evolution of the angular frequency of rotation between models with 5 $M_{\odot}$ computed in this work (solid lines) and Anderson et al. (2016) models of similar composition and mass (dashed line), for two rotation rates.

Chapter 4

Period Change Rates using MESA

This section describes how PCRs were obtained using the RSP functionality of MESA. These rates were calculated for each evolutionary track shown in the previous section. We studied the effect of the increase in the rotation rate and the calculated rates were compared with the PCRs for classical LMC Cepheids, as recently obtained by Rodríguez-Segovia et al. (in prep.).

4.1 Radial Stellar Pulsation - RSP

RSP is a recent functionality added to MESA (Smolec & Moskalik 2008; Paxton et al. 2019) that models high-amplitude, self-excited, non-linear pulsations that the star develops when it crosses the IS. RSP performs three operations: it generates an initial model of the envelope, performs a linear non-adiabatic stability analysis on the model, and integrates the time-dependent non-linear equations. As a result, we obtain a model of the nonlinear radial pulsations, growth rates of the three lowest-order radial pulsation modes, and linear periods of the excited pulsation modes.

Since the inner parts of the star do not participate in the oscillations of classical pulsators, a complete stellar model is not necessary (Smolec & Moskalik 2008; Paxton et al. 2019). Therefore, RSP is currently limited to pulsations determined by the structure

of the star's envelopes. RSP starts by creating a chemically homogeneous model of the envelope for certain given stellar parameters (M, L, $T_{\rm eff}$, X and Z). We choose these input parameters from our evolutionary tracks, guided by approximate IS edges provided in the MESA test suite `rsp_check_2nd_crossing`. The initial RSP model depends on equations describing time-dependent convection, described in Smolec & Moskalik (2008), which also depend on free parameters that are listed in Table 3 of Paxton et al. (2019). Pulsation periods depend weakly on these parameters. However, period growth rates and light curves are sensitive to the choice of these convective variables. In Table 4 of Paxton et al. (2019) are shown different sets for these parameters. Set A corresponds to the simplest convective model, set B adds radiative cooling, while set C adds turbulent pressure and turbulent flux. Set D, which includes these same effects in addition to radiative cooling, showed convergence problems and was therefore discarded. A comparison of convective parameter sets is made in Subsection 4.2.1

The non-adiabatic linear analysis is performed on the initial model using the linearized RSP equations (details in Smolec 2009). These provide the eigenmodes, periods, and growth rates. The initial static model is perturbed with a linear combination of the velocity eigenmodes of the three lowest-order radial modes.

The time integration is performed for a specific number of cycles. A new cycle begins when the model passes through the maximum radius. In general, we found a good agreement between the periods of the fundamental mode obtained in the linear analysis and after 500 cycles of time integration. However, the effects of double-mode pulsations are not considered in the linear periods. Especially in first crossing Cepheids, we observe that the fundamental mode and first overtone mode are often both simultaneously excited. In some of these cases, although the pulsations tends to converge to a single mode of pulsation, the period does not remain stable after several pulsation cycles. Since integration over time for a given number of cycles for all evolutionary tracks is highly time-consuming, we consider the periods obtained in the linear non-adiabatic analysis to perform the calculation of PCRs.

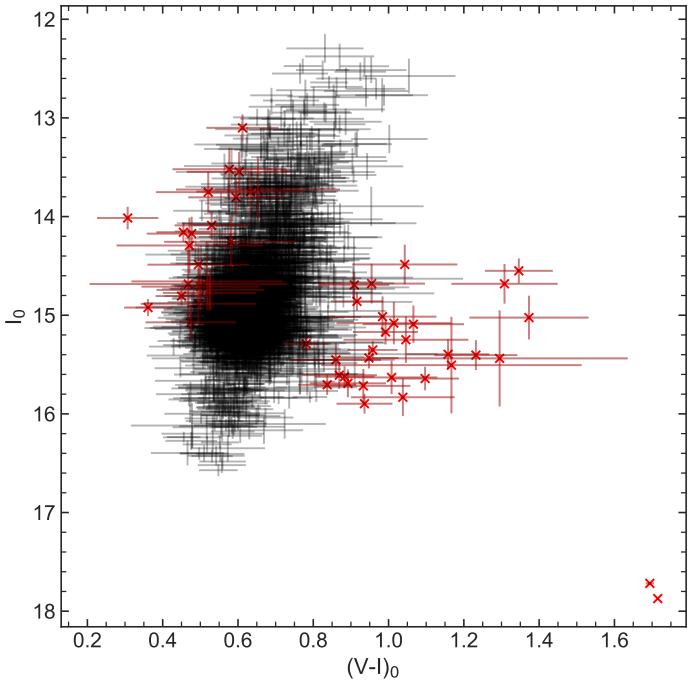

Figure 4.1: Color-magnitude diagram with data for fundamental-mode classical Cepheids of the LMC from the OGLE-IV catalog of variable stars. Data in red were discarded following the method described in Madore et al. (2017), while classical Cepheids in black were used in this work.

4.2 Periods of the Fundamental Mode of Pulsation

The edges of the IS for the fundamental mode were obtained with RSP, and are tabulated in Table 4.1. We found that there is no dependence of these edges on the rotation rate, but they are sensitive to the choice of the convective parameters of RSP, as mentioned in Paxton et al. (2019).

4.2.1 Comparison of Convective Parameter Sets

In order to compare the convective parameter sets A and C, we use data of fundamental-mode classical Cepheids in the LMC from the OGLE-IV variable stars catalog (Soszyński et al. 2015), corrected by extinction using the optical reddening map presented in Skowron et al. (2021), data with a high vertical dispersion in the Wesenheit P-L relationship were

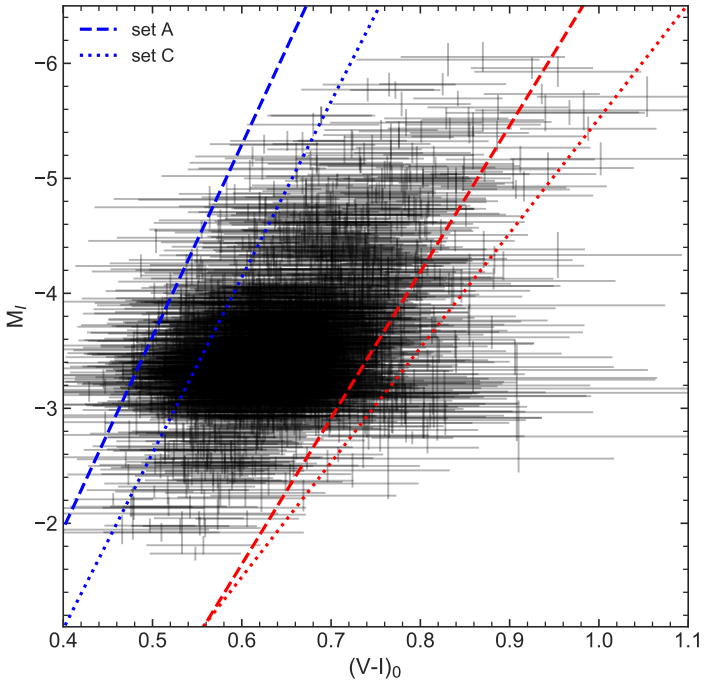

Figure 4.2: Color-magnitude diagram comparing the blue and red edges of the IS of the fundamental mode of pulsation for two different sets of convective parameters, namely set A (dashed lines) and set C (dotted lines). Data for fundamental-mode classical Cepheids of the LMC from the OGLE-IV catalog of variable stars are shown as dots.

not considered.. The mean I and V magnitudes are obtained by means of a light curve integration (Soszynski et al. 2008). In addition, following the method described in Madore et al. (2017), some data were discarded due to their high vertical deviation in a diagram of the magnitude residuals of the P-L relation versus the corresponding residual of the Wesenheit P-L relation. These deviations are possibly due to errors in the individual extinctions adopted, Figure 4.1 shows the discarded data. Distances to the stars, used to calculate their absolute magnitudes, were obtained from Jacyszyn-Dobrzeniecka et al. (2016). The edges of the IS calculated using set A and set C of convective parameters tabulated in Paxton et al. (2019) are shown in Figure 4.2. We note that the IS of set C is bluer than that of set A, containing 87% and 94% of the Cepheid sample, respectively. In spite of this, we adopted the convective parameters of set C since they are more physically

Z	$\alpha_{\rm blue}$	$\beta_{\rm blue}$	$\alpha_{\rm red}$	$\beta_{\rm red}$
0.005	-32.29	125.61	-22.27	86.24
0.007	-25.86	101.09	-13.51	53.36
0.009	-24.12	94.40	-13.64	53.83

Table 4.1: Coefficients of the red and blue edges of the IS, assuming $\log(L/L_\odot) = \alpha \log T_{\rm eff} + \beta$, for three metallicities, namely $Z = 0.005$, 0.007, and 0.009.

representative. However, a combination of these sets is needed to contain all the classical Cepheid sample of the OGLE-IV catalog, which will be done in future work.

4.2.2 Linear Periods of the Fundamental Mode

Linear periods for the fundamental mode were calculated for each evolutionary track crossing the IS. These are shown in Figure 4.3. The time scales are of the order of ~ 0.02, 0.4, and 0.7 Myr for the 1st, 2nd, and 3rd crossing, respectively. Given this fast evolution, especially at the first crossing of the IS, it is not possible to appreciate a temporal variation in Figure 4.3. However, the change in the period during these crossings is appreciable, being greater for higher mass stars since the blue loop extension is greater for these stars.

As mentioned in previous sections, during the first and third crossings the period increases, while during the second crossing the period decreases. It can also be noted that as the rotation rate increases, a Cepheid of a given mass tends to reach a longer period at the beginning of the IS (second crossing) and at the end of the IS (first and second crossings). This can be understood in terms of the period-luminosity relation: since rotating tracks are more luminous than non-rotating tracks, the latter can be expected to have shorter periods. As shown in Figure 3.4, for $\omega_0 > 0.5$, the blue loops of tracks with $4\,M_\odot$ are outside the IS, hence the pulsations are not excited in these models. Note that the period ranges that we obtain are in agreement with those shown in Figure 5 of Anderson et al. (2016), for an adopted metallicity of $Z = 0.007$, similar to the one adopted in their work.

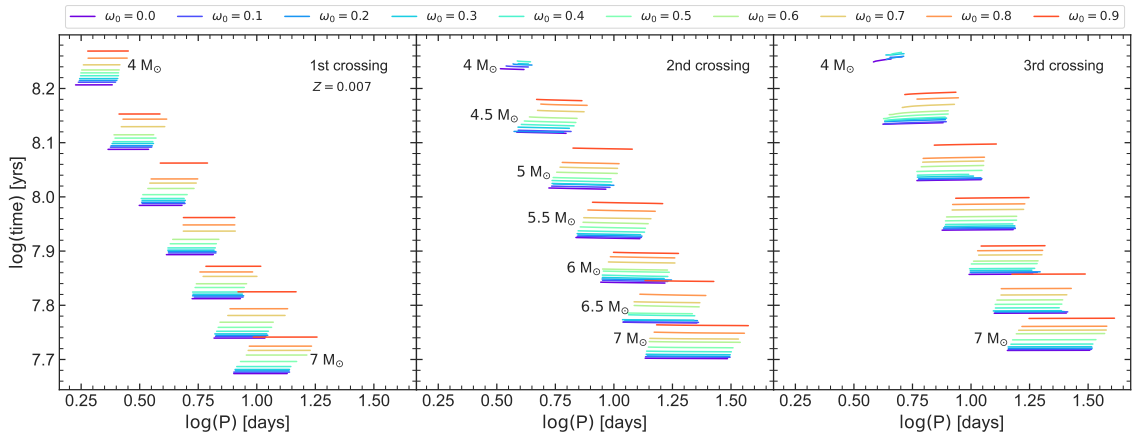

Figure 4.3: Time as a function of the linear periods obtained with RSP. Periods are shown for the first crossing (left panel), second crossing (middle panel), and third crossing (right panel). Periods for masses, from top to bottom, from 4 to 7 $M_\odot$ in steps of 0.5 $M_\odot$ are displayed in each panel. Lines of different colors correspond to different ω_0, following the color scheme given at the top of this figure.

4.2.3 Period-Age and Period-Age-Temperature Relations

Cepheids obey period-age and period-color-age relations (see, e.g., Kippenhahn & Smith 1969; Bono et al. 2005). Considering the mass-luminosity (Eddington 1924) and P-L relation, Cepheids with a high initial mass, a high luminosity and, consequently, a long period are younger than low-mass Cepheids with lower luminosity and, therefore, a shorter period. In addition, the period increases toward the red edge of the IS.

We fit period-age relations to the periods obtained for each crossing by performing an ordinary least-squares regression; these are shown in Figure 4.4. We show relations for $Z = 0.007$ with $\omega_0 = 0.0$, 0.5, 0.9, and relations averaged in rotation for metallicities $Z = 0.005$, 0.007, and 0.009, respectively. We noted dependencies with four important parameters: crossing number, since the three crossings occur in sequence and the time scales of the first crossing are much shorter than those of the second and third crossings, resulting in slightly steeper relations; position in the IS, due to the change of the pulsation period produced by the expansion or compression of the star and the extent of the IS

by itself, producing appreciable changes in slope and zero point; rotation, since these models have a longer MS due to rotational mixing, causing a significant change in age in fast-rotating stars; metallicity, which produces appreciable changes in the age of the star for short pulsation periods, similar to the effect produced by rotation in stars with longer periods. The period-age relations obtained for the red and blue edges, in addition to an average relation, are tabulated in Table 4.2. We also included period-age-temperature relations, where the temperature is a proxy for the color of the star. These relations take into account the temperature width of the IS, resulting in a better representation of the age of the star. In general, the residuals of these relationships are small, less than 0.04 dex in log-age.

In Figure 4.5 we compare our results with the period-age relations with averaged initial rotation obtained by Anderson et al. (2016). Appreciable differences are observed for short-period stars, which are a consequence of the difference in adopted metal content, in addition to the different implementations of rotation i in the MESA and Geneva codes.

4.2.4 Period-Luminosity and Period-Luminosity-Temperature Relations

In Figure 4.6, period-luminosity (P-L) relations for absolute magnitudes in the *I* band, as it is one of the bands used by the OGLE catalog, are shown. In the upper panel, we compare the effects caused by rotation, while in the lower panel we compare the effects produced by metallicity on non-rotating models. These relationships have slightly larger residuals than the age-period and age-period-temperature relationships, of the order of 0.1 dex in log-luminosity. We note that rotation tends to slightly broaden the width of the P-L relation, both for short and long periods, but the broadening is minimum for periods close to 10 days. This complex behavior is due to the non-monotonic relationship between rotation and luminosity, due to the competition between rotational mixing and the centrifugal force. On the other hand, considering a wider range in metallicity in the fit of

ω_0	Crossing	$\alpha_{\rm blue}$	$\beta_{\rm blue}$	$\alpha_{\rm red}$	$\beta_{\rm red}$	α	β
0.0	1st	-0.78	8.38	-0.71	8.47	-0.74	8.43
	2nd	-0.83	8.63	-0.62	8.61	-0.71	8.62
	3rd	-0.85	8.70	-0.65	8.70	-0.74	8.70
0.5	1st	-0.79	8.42	-0.71	8.51	-0.74	8.46
	2nd	-0.80	8.62	-0.64	8.67	-0.71	8.65
	3rd	-0.74	8.61	-0.68	8.76	-0.71	8.69
0.9	1st	-0.73	8.47	-0.64	8.54	-0.68	8.51
	2nd	-0.80	8.73	-0.61	8.72	-0.70	8.72
	3rd	-0.76	8.73	-0.62	8.77	-0.69	8.75
Z	Crossing	$\alpha_{\rm blue}$	$\beta_{\rm blue}$	$\alpha_{\rm red}$	$\beta_{\rm red}$	α	β
0.005	1st	-0.82	8.45	-0.74	8.56	-0.78	8.51
	2nd	-0.72	8.65	-0.69	8.76	-0.71	8.71
	3rd	-0.88	8.80	-0.77	8.89	-0.82	8.84
0.007	1st	-0.76	8.42	-0.68	8.51	-0.72	8.47
	2nd	-0.81	8.66	-0.63	8.67	-0.71	8.66
	3rd	-0.78	8.68	-0.65	8.74	-0.71	8.72
0.009	1st	-0.72	8.37	-0.64	8.44	-0.68	8.40
	2nd	-0.73	8.55	-0.58	8.58	-0.65	8.57
	3rd	-0.72	8.60	-0.61	8.66	-0.66	8.63

Table 4.2: Period-age relationship ($\log(\text{age/year}) = \alpha \log(\text{P/days}) + \beta$) coefficients. The top four rows correspond to coefficients for the blue edges ($\alpha_{\rm blue}$ and $\beta_{\rm blue}$), red edges ($\alpha_{\rm red}$ and $\beta_{\rm red}$) and an average of the IS (α and β), calculated for three rotation rates $\omega_0 = 0.0$, 0.5 and 0.9, for three crossings of the IS, and $Z = 0.007$. The lower four rows correspond to these coefficients calculated for three metallicities, namely $Z = 0.005$, 0.007 and 0.009, averaged over rotation.

Z	Crossing	α	β	γ
0.005	1st	-0.87	-3.0	19.84
	2nd	-0.92	-3.39	21.57
	3rd	-0.98	-3.87	23.45
Z	Crossing	α	β	γ
0.007	1st	-0.90	-3.03	19.96
	2nd	-0.91	-3.51	21.95
	3rd	-0.92	-3.58	22.27
Z	Crossing	α	β	γ
0.009	1st	-0.88	-2.88	19.35
	2nd	-0.85	-3.16	20.57
	3rd	-0.87	-3.29	21.1

Table 4.3: Period-age-temperature relationship ($\log(\text{age/year}) = \alpha \log(\text{P/days}) + \beta \log(\text{T}_{\text{eff}}/\text{K}) + \gamma$) coefficients, for $Z = 0.007$, averaged over rotation and for each crossing of the IS.

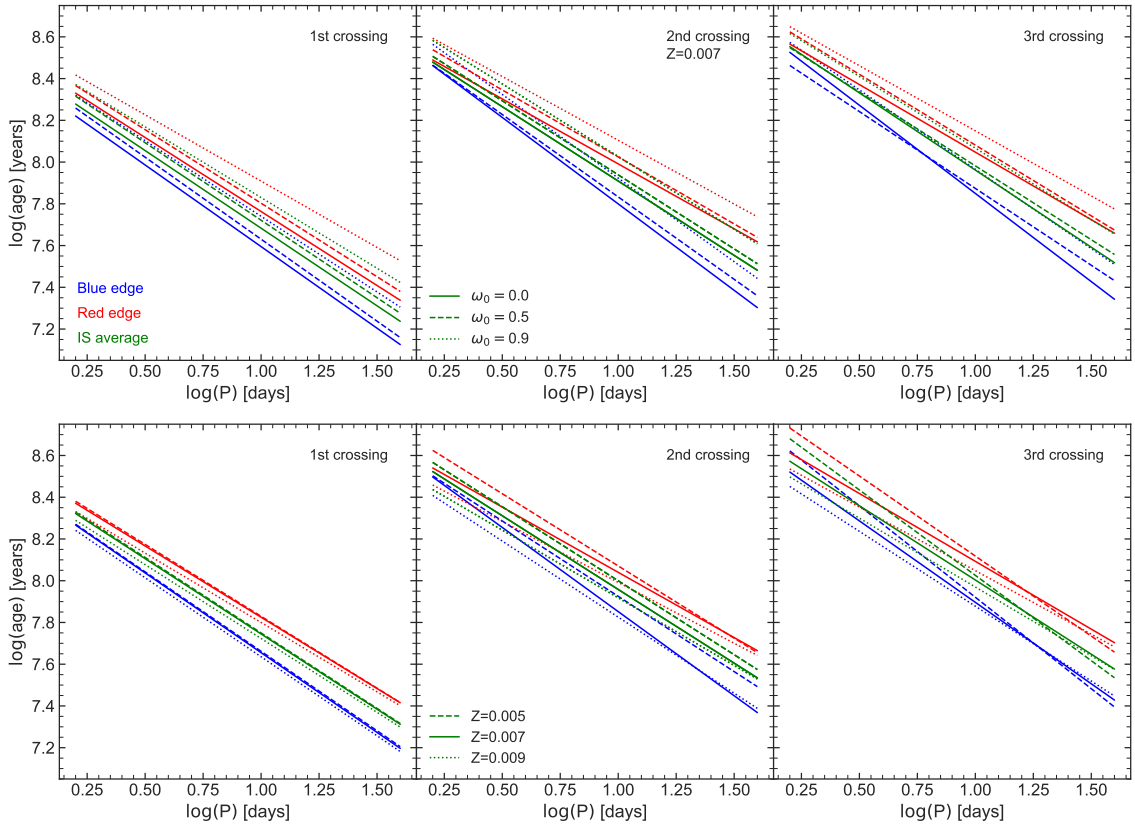

Figure 4.4: Period-age relationships obtained from the linear periods calculated with RSP. This relationship was calculated for the first crossing (left panels), second crossing (middle panels), and third crossing (right panels). The upper panels show the relationships for three initial rotation rates $\omega_0 = 0.0$ (solid line), 0.5 (dashed line), and 0.9 (dotted line), considering $Z = 0.007$. The lower panels show the relationships for three different metallicities, namely $Z = 0.005$, 0.007, and 0.009. In each panel, the period-age relationship for the blue (blue lines) and red (red lines) edges of the IS, as well as for an average over the IS (green lines), are shown.

the P-L relationship produces a widening on this relationship, which however is minimal during the first crossing of the IS.

A comparison of our P-L relationships with those from Anderson et al. (2016) in the V band is shown in Figure 4.7, for the three crossings of the IS and averaged over rotation. We note that in general, the blue and red edges of Anderson's models are brighter than those obtained in this work. For the first crossing, this effect is more noticeable for longer

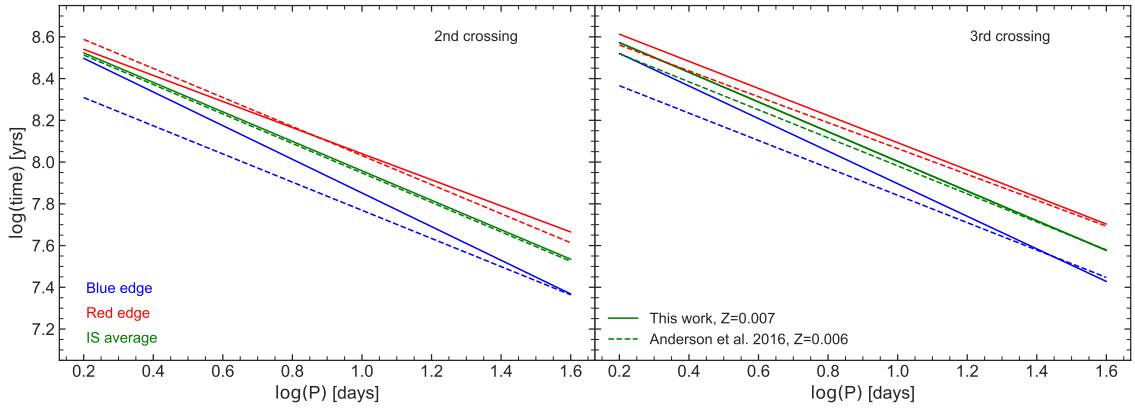

Figure 4.5: Comparison of period-age relationships of this work (solid lines) with those presented by Anderson et al. (2016) (dashed lines), for the second (left panel) and third (right panel) crossings of the IS. In each panel, the period-age relationship for the blue (blue lines) and red (red lines) edges of the IS, as well as an average over the IS (green lines), are shown

periods, while for the second and third crossings, the difference in luminosity is notably higher for the short periods of the blue edge and decreases for longer periods. In the same way as for the period-age-temperature relations, we tabulate the coefficients of the period-luminosity-temperature relations in Table 4.5.

4.3 Period Change Rates

PCRs due to evolution were calculated directly from the linear periods obtained with RSP, and are shown in Figure 4.8. The behavior of the blue loops in the HRD define the shapes of the PCR vs. period curves; in the case of stars of 4 $M_{\odot}$, the blue loops showed a complex behavior due to a large number of He-spikes, which is reflected in the curves of the second and third crossings, where $\log(dP/dt)$ shows a behavior with a similar degree of complexity. We note a dependence of the PCR with rotation. First-crossing non-rotating models tend to have a higher $\log(dP/dt)$ at the beginning of the IS than rotating models, but the models with the highest rotation rate are those with the highest $\log(dP/dt)$ at the red end of the IS. In the case of the second and third crossing curves, in most cases,

ω	Crossing	$\alpha_{\rm blue}$	$\beta_{\rm blue}$	$\alpha_{\rm red}$	$\beta_{\rm red}$	α	β
0.0	1st	-3.24	-1.96	-2.85	-1.60	-3.07	-1.75
	2nd	-3.47	-1.59	-2.56	-1.67	-3.18	-1.46
	3rd	-3.53	-1.49	-2.50	-1.72	-3.12	-1.46
0.5	1st	-3.26	-1.94	-2.84	-1.60	-3.08	-1.73
	2nd	-3.21	-1.82	-2.55	-1.69	-2.93	-1.66
	3rd	-3.17	-1.84	-2.57	-1.63	-2.90	-1.66
0.9	1st	-3.23	-1.93	-2.74	-1.62	-2.99	-1.75
	2nd	-3.34	-1.65	-2.46	-1.77	-2.97	-1.58
	3rd	-3.27	-1.68	-2.42	-1.81	-3.12	-1.41
Z	Crossing	$\alpha_{\rm blue}$	$\beta_{\rm blue}$	$\alpha_{\rm red}$	$\beta_{\rm red}$	α	β
0.005	1st	-3.32	-1.91	-3.00	-1.49	-3.15	-1.69
	2nd	-2.97	-1.88	-2.79	-1.43	-2.88	-1.64
	3rd	-3.41	-1.52	-2.91	-1.28	-3.15	-1.39
0.007	1st	-3.24	-1.94	-2.81	-1.61	-3.05	-1.74
	2nd	-3.34	-1.69	-2.52	-1.71	-3.03	-1.57
	3rd	-3.32	-1.67	-2.50	-1.72	-3.04	-1.51
0.009	1st	-3.20	-1.97	-2.66	-1.75	-2.91	-1.85
	2nd	-3.15	-1.86	-2.43	-1.83	-2.75	-1.84
	3rd	-3.14	-1.84	-2.39	-1.89	-2.74	-1.85

Table 4.4: I-band period-luminosity relation (in the form $M_I = \alpha \log(P/\text{days}) + \beta$) coefficients. The top four rows correspond to coefficients for the blue edges ($\alpha_{\rm blue}$ and $\beta_{\rm blue}$), red edges ($\alpha_{\rm red}$ and $\beta_{\rm red}$), and an average over the IS (α and β), calculated for three initial rotation rates (ω_0 = 0.0, 0.5, and 0.9), for three crossings of the IS, and Z = 0.007. The bottom four rows correspond to these same coefficients, but calculated for three metallicities, namely Z = 0.005, 0.007, and 0.009, averaged over rotation.

Z	Crossing	α	β	γ
0.005	1st	-3.71	-12.63	46.08
	2nd	-3.78	-14.50	53.31
	3rd	-3.79	-14.60	53.72
Z	Crossing	α	β	γ
0.007	1st	-3.80	-12.85	46.95
	2nd	-3.73	-14.71	54.02
	3rd	-3.73	-14.85	54.56
Z	Crossing	α	β	γ
0.009	1st	-3.78	-12.74	46.50
	2nd	-3.68	-14.31	52.45
	3rd	-3.67	-14.48	53.10

Table 4.5: Period-luminosity-temperature relation (in the form $M_I = \alpha \log(P/\text{days}) + \beta \log(T_{\text{eff}}/\text{K}) + \gamma$) coefficients, for $Z = 0.007$, averaged over rotation and for each crossing of the IS.

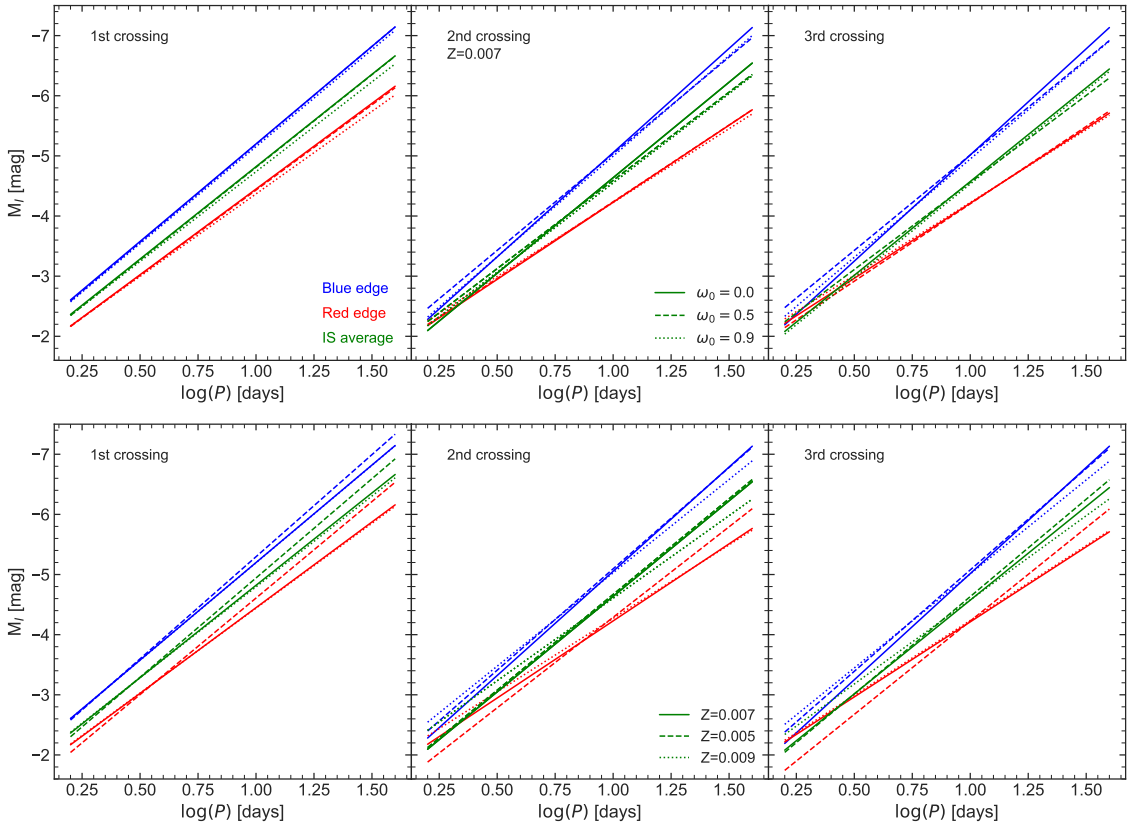

Figure 4.6: Period-luminosity relationships obtained from the linear periods calculated with RSP. This relationship was calculated for the first crossing (left panels), second crossing (middle panels) and third crossing (right panels). The upper panels show the relationships for three initial rotation rates ω_0 = 0.0 (solid line), 0.5 (dashed line) and 0.9 (dotted line), considering Z=0.007. The lower panels show the relationships for three different metallicities, namely Z = 0.005, 0.007 and 0.009. In each panel, period-luminosity relationship for the blue (blue lines), red (red lines) edge of the IS, and an average (green lines) in the IS are shown.

non-rotating tracks have a higher rate of period change during the entire crossing of the IS, whereas the dependence on rotation is not monotonic in the case of the second crossing.

For 5 $M_\odot$ stars with ω_0 = 0.4 at the third crossing, a small bump in luminosity during this stage causes a large increase in the rate of period change, which reaches the area of the first crossing. In Figure 4.9 we add dotted lines corresponding to the PCRs of the fourth and fifth crossings of 5 $M_\odot$ stars. The PCR of the fourth crossing is negative, but

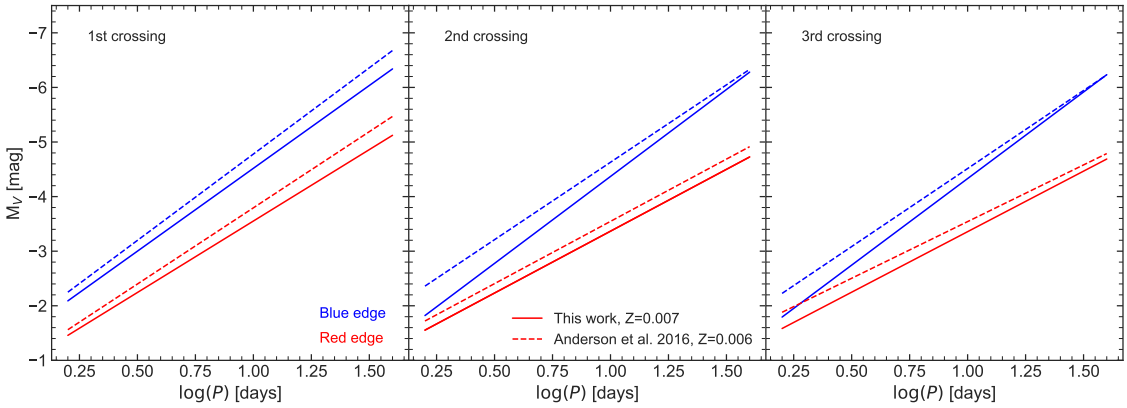

Figure 4.7: Comparison of period-luminosity relationships of this work (solid lines) with those presented by Anderson et al. (2016) (dashed lines), for the first (left panel), second (central panel), and third (right panel) crossings of the IS. In each panel, the period-luminosity relationships for the blue (blue lines) and red (red lines) edges of the IS are shown

it is higher by more than an order of magnitude, in absolute value, than the rate of the second crossing. On the contrary, the rate of the fifth crossing is positive and is blended with the rate of the third crossing. The typical duration of the fourth crossing is roughly twice the timescale of the first crossing of the IS, while the duration of the fifth crossing is comparable to that of the third crossing of the IS. Nevertheless, if irregularities in the HRD, such as those produced by a fourth crossing of the IS, are real, perhaps attributed to mixing episodes that may inject a reasonable amount of helium into the core, they may produce potentially observable effects in PCRs, in spite of the very short duration of these events.

In addition, we include the PCRs for models with $Z = 0.005$ and 0.009 in Figure 4.10. During the first crossing the behavior is more regular, being the models with lower metallicity the ones with slightly higher $\log(dP/dt)$. For the second crossing, the behavior is reversed, being the models with higher metallicity the ones that present higher $\log(dP/dt)$. In the case of the third crossing, the behavior is more irregular, high mass models with $Z = 0.007$ tending to show a higher rate of period change, while in models with lower mass the highest rate of period change is observed with a metallicity of $Z = 0.005$. The duration

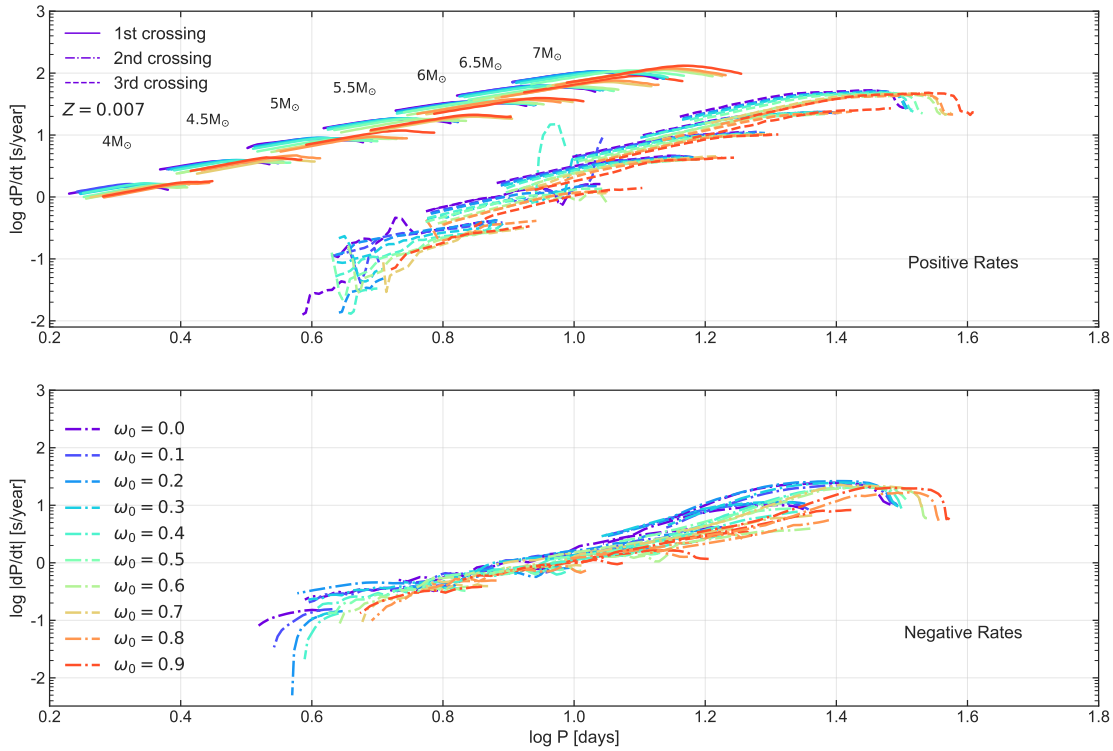

Figure 4.8: PCRs as a function of the period for evolutionary tracks with $Z = 0.007$. The upper panel shows positive rates corresponding to the first (solid lines) and third (dashed lines) crossings of the IS. The lower panel shows negative rates corresponding to the second (dashed-dotted lines) crossing of the IS. For each panel, curves are shown for masses, from left to right, between 4 and 7 $M_{\odot}$, in steps of 0.5 $M_{\odot}$. Lines of different colors correspond to different ω_0 values, following the color scheme given at the left of the lower panel.

of the first crossing increases slightly as metallicity increases, while the time scale of the second crossing increases as Z decreases. This does not hold for the third crossing, where the behavior is non-monotonic, with models with $Z = 0.005$ having the longest time scale. The behavior of PCRs is associated with these differences between the time scales of the crossings.

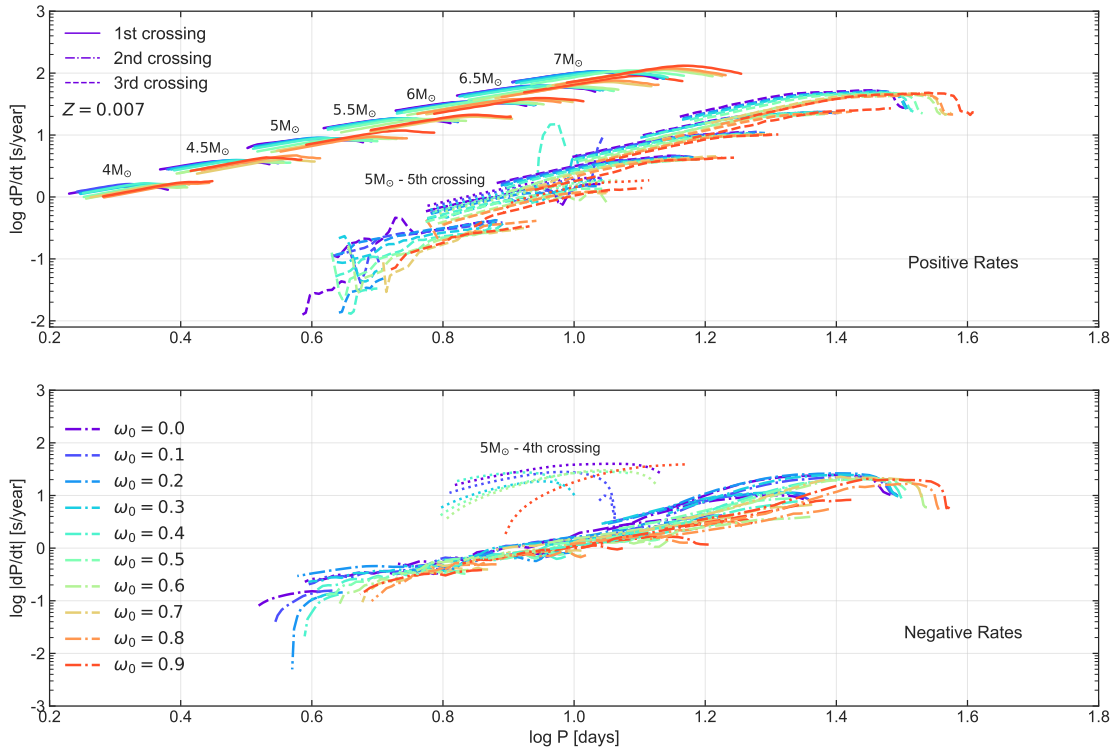

Figure 4.9: PCRs as a function of the period for evolutionary tracks with $Z = 0.007$. The upper panel shows positive rates corresponding to the first (solid lines), third (dashed lines) and fifth (dotted lines) crossings of the IS. The lower panel shows negative rates corresponding to the second (dashed-dotted lines) and fourth (dotted lines) crossing of the IS. For each panel, PCRs are shown for masses from left to right, from 4 to 7 $M_{\odot}$ in steps of 0.5 $M_{\odot}$. Lines of different colors correspond to different ω_0, following the color scheme given at the left of the lower panel.

4.4 Comparison with Empirical PCRs

Cepheids are dubbed "magnifying glasses of stellar evolution" (Kippenhahn & Weigert 1994) because they provide a highly sensitive test of stellar evolution. Therefore, it is essential to compare theoretical results with empirical data for actual Cepheids, in order to gain insight into the adequacy of the input physics that is used to build these models. It is of particular interest to compare the results obtained by us and previous authors with data for classical Cepheids in the LMC, given the large amount of data currently available.

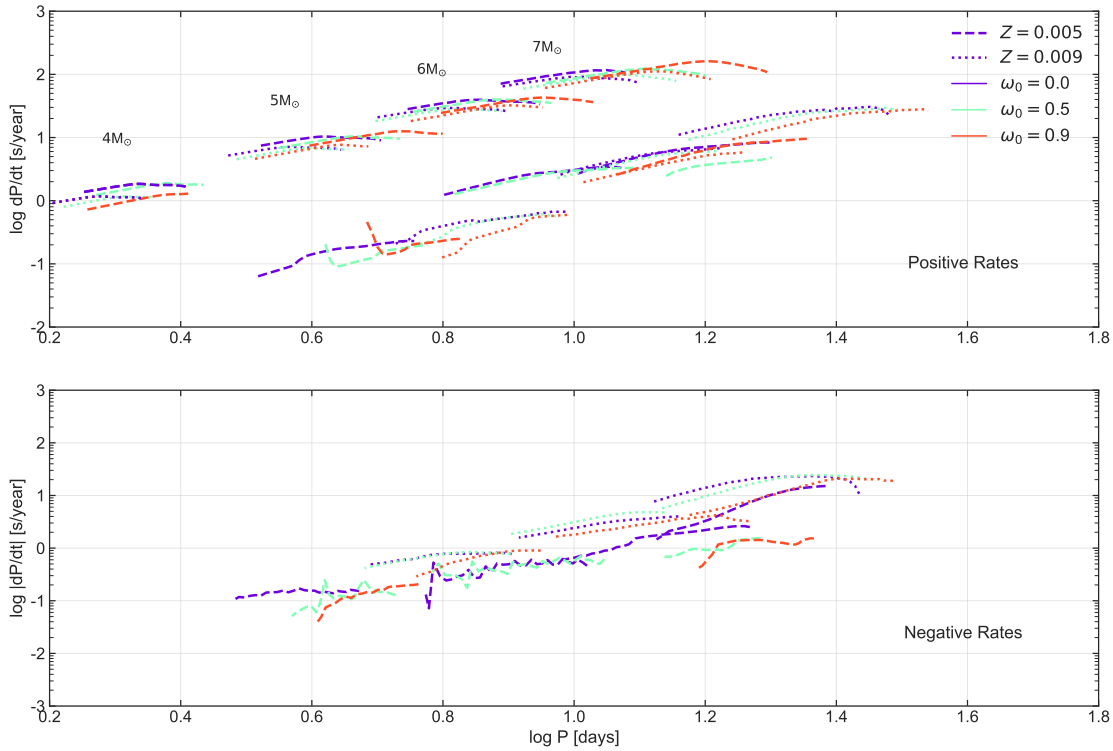

Figure 4.10: PCRs as a function of the period for evolutionary tracks with $Z = 0.005$ (dashed lines) and 0.009 (dotted lines). The upper panel shows positive rates corresponding to the first (upper lines) and third (lower lines) crossings of the IS. The lower panel shows negative rates corresponding to the second crossing of the IS. In each panel, PCRs are shown for masses, from left to right, from 4 to 7 $M_{\odot}$, in steps of 1 $M_{\odot}$. Lines of different colors correspond to different ω_0 values, following the color scheme given at the right of the upper panel.

Rodríguez-Segovia et al. (in prep.) have recently computed PCRs for an unprecedented number of LMC Cepheids, making it a key work for comparison with model predictions.

Figure 4.11 shows our PCRs for models with $Z = 0.007$ and the empirical values obtained by Rodríguez-Segovia et al. (in prep.), in units of s/yr. The same comparison is made with models with metallicities $Z = 0.005$ and $Z = 0.009$, shown in Figure 4.12. There is good agreement between the models and the data, but there are several points to note. In the area of positive rates and short periods of Figure 4.11, models with $Z = 0.007$ do not cover the data for the shortest-period Cepheids. Models with the same metallicity but

masses lower than 4 $M_\odot$ could in principle cover this low-period regime. However, with the adopted input physics, we were unable to produce models with $< 4\,M_\odot$ that crossed the IS during core He burning, as these models produced blue loops that were too short, similarly to what was previously found by Anderson et al. (2016). Models with different metallicity cover a wider range of periods. This difference is not as noticeable in the negative rate panel of Figures 4.11 and 4.12, where the PCR of the 4 $M_\odot$ model do cover the area of the shortest periods. On the other hand, in the long period region, a couple of Cepheids with implied masses greater than 7 $M_\odot$ are observed, which makes them interesting sources since the vast majority of Cepheid masses measured lie between 3.6 and 5 $M_\odot$ (Pilecki et al. 2018; Evans et al. 2018; Gallenne et al. 2019). Most of the data sample are classical Cepheids with implied masses near and below 4 $M_\odot$, with a vast variety of possible initial rotation rates. Several data points are below (e.g., the long-period region at the third crossing) or slightly above (between $\log P = 0.6$ and 1.1) the loci predicted by our models. This can also be seen in Figure 4.13, where a line was fitted to the models, considering tracks of the second and third crossing, of all masses and rotation rates calculated in this work. The dispersion of the models and the data of Rodríguez-Segovia et al. (in prep.) was calculated with respect to the fitted line for models with $Z = 0.007$, and $Z = 0.005$ and 0.009, separately. We note that, considering the full range of periods of the data, 72.2% of the sample of Rodríguez-Segovia et al. (in prep.) fall within the 3-sigma range of the models, averaged over metallicity and IS crossings. The former percentage takes into account the short-period Cepheid data that are not covered by our models. A complication that follows from Figures 4.11 and 4.12 is that there is a degeneracy in these models, since a curve with a certain mass, metallicity, and initial rotation rate can be overlapped by a curve with a different combination of these parameters. A denser grid in metallicity and masses is needed to cover the full range of the Rodríguez-Segovia et al. (in prep.) data.

Anderson et al. (2016) present PCRs for $Z = 0.006$. Despite the difference in metal content with respect to our models, when compared to our values for models with $Z = 0.007$, one finds good agreement for the positive rates. In the case of negative rates, on

the other hand, the differences reach up to an order of magnitude. The main reason for the discrepancies in absolute PCR values is the different implementations of rotation and the different input parameters between the MESA and Geneva codes, as mentioned in Section 3.2.

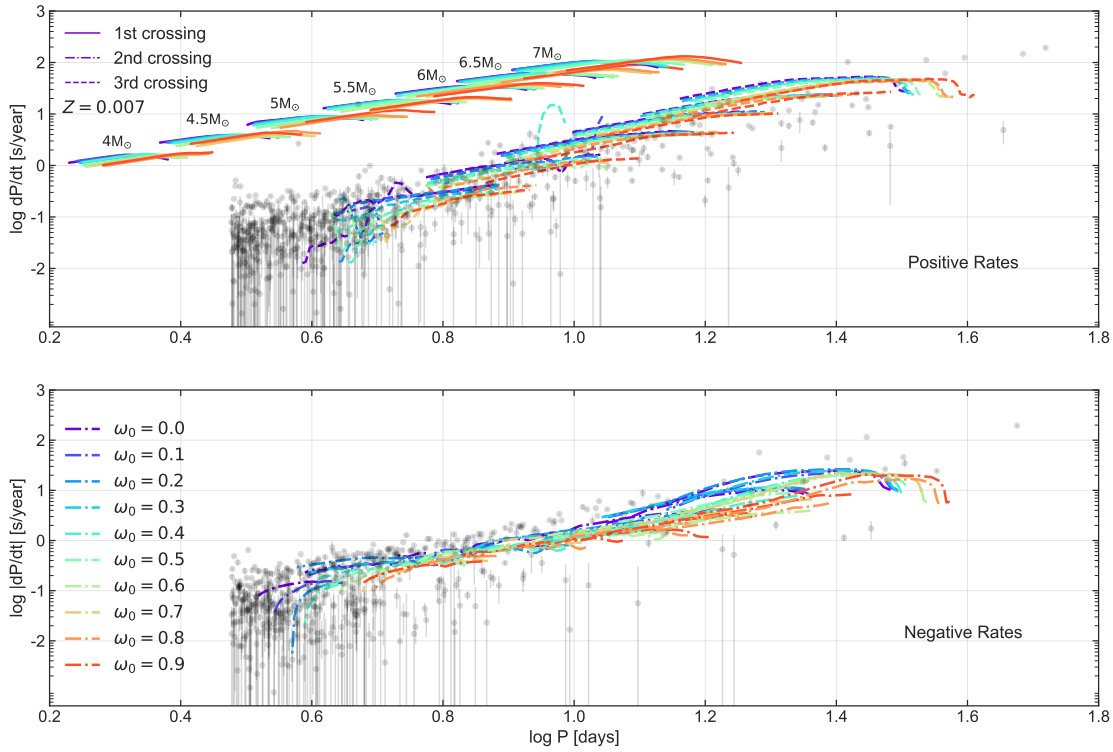

Figure 4.11: Comparison between the PCRs for models with $Z = 0.007$ obtained in this work and the empirical rates calculated by Rodríguez-Segovia et al. (in prep.) for LMC Cepheids. The upper panel shows positive rates corresponding to the first (solid lines) and third (dashed lines) crossings of the IS. The lower panel shows negative rates corresponding to the second crossing of the IS (dashed-dotted lines). In each panel, PCRs are shown for masses, from left to right, from 4 to 7 $M_{\odot}$, in steps of 0.5 $M_{\odot}$. Lines of different colors correspond to different ω_0 values, following the color scheme given at the left of the lower panel.

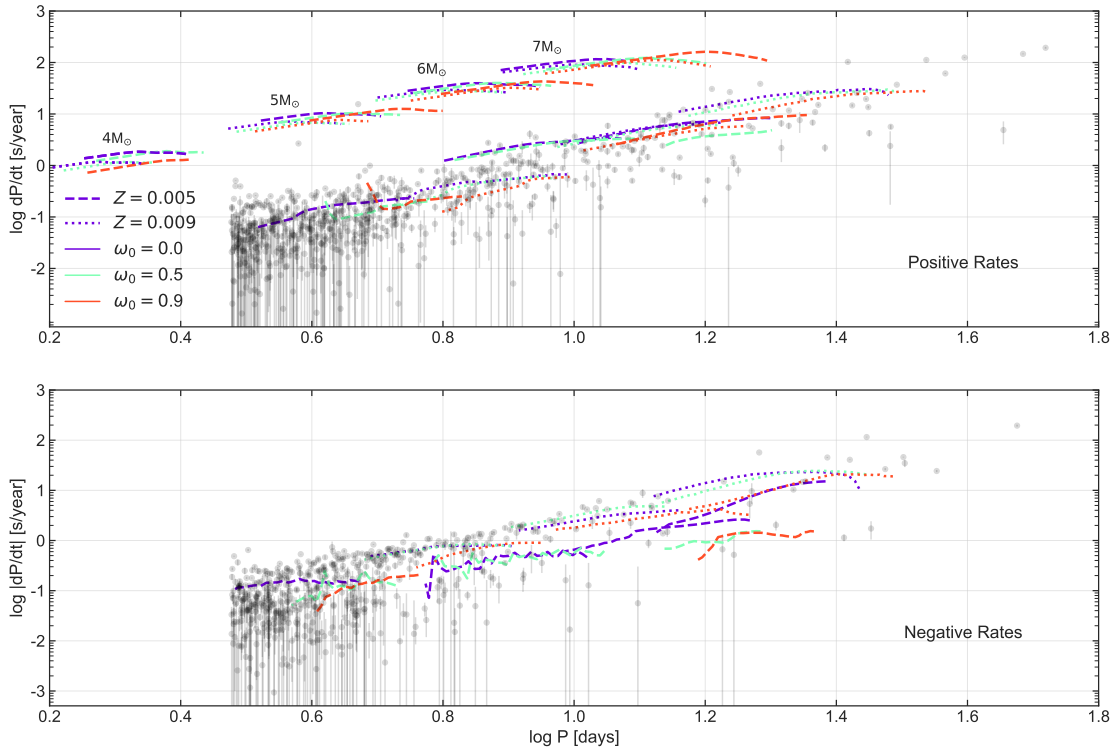

Figure 4.12: Comparison between the PCRs for models with $Z = 0.005$ (dashed lines) and $Z = 0.009$ (dotted lines) obtained in this work and the empirical rates calculated by Rodríguez-Segovia et al. (in prep.) for LMC Cepheids. The upper panel shows positive rates corresponding to the first (upper left part) and third (lower right part) crossings of the IS. The lower panel shows negative rates corresponding to the second crossing of the IS. For each panel, PCRs are shown for masses, from left to right, from 4 to 7 $M_{\odot}$, in steps of 1 $M_{\odot}$. Lines of different colors correspond to different ω_0 values, following the color scheme given at the right of the upper panel.

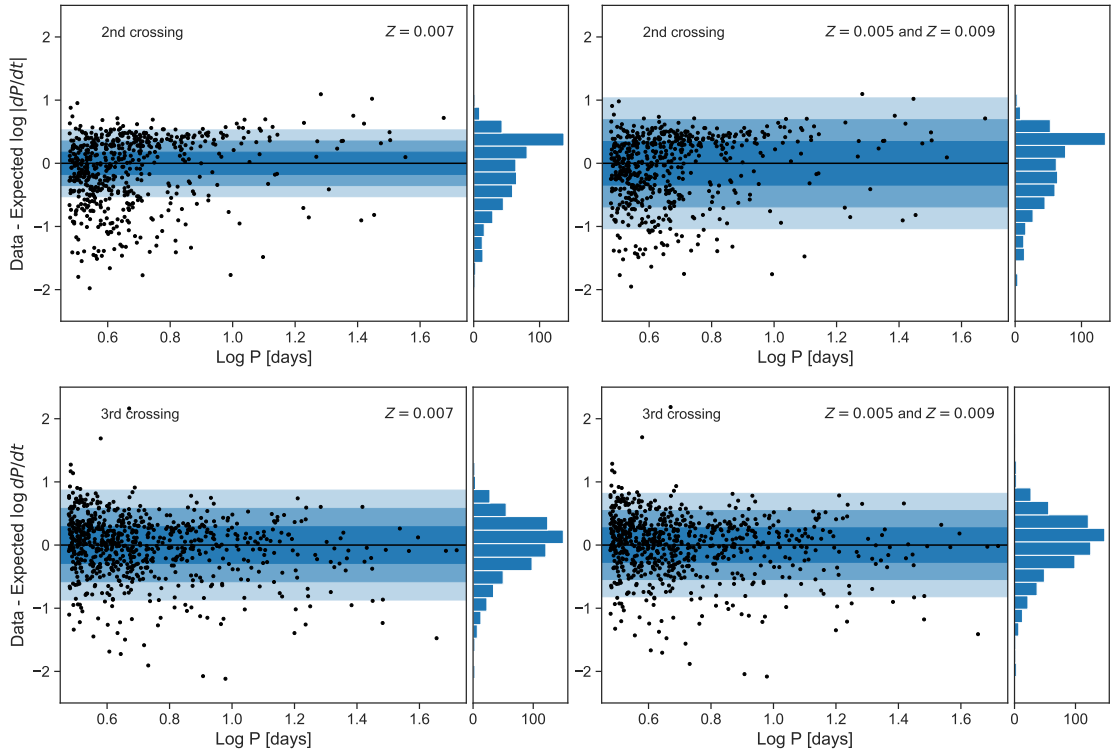

Figure 4.13: Residuals with respect to a linear fit made to the PCRs calculated with MESA. Upper panels show residuals of second crossing models, whereas lower panels show residuals of third crossing models. Residuals of models with $Z = 0.007$ are shown in the left panel, while residuals of models with $Z = 0.005$ and 0.009 are shown in the right panel. Shaded areas represent one, two, and three standard deviations, in order of decreasing transparency, of the PCRs with respect to the linear fit. A histogram of the residuals is presented in each panel for better visualization.

Chapter 5

Conclusions

In this thesis, we use the stellar evolution code MESA to calculate PCRs for a set of evolutionary models of intermediate-mass stars. These models span a mass range between 4 and 7 $M_\odot$; a metallicity of $Z = 0.005$, 0.007, and 0.009; and an initial rotation rate between $\omega_0 = 0.0 - 0.9$.

Rotation has a major impact on the evolution of a star. At the beginning of the MS, because the centrifugal force decreases the effective gravitational acceleration, a rotating model has a lower effective temperature than a non-rotating model, reaching a temperature difference of up to $\sim$ 1700 K. During the MS, the centrifugal force produces additional gravity support, which decreases the luminosity and size of the core. At the same time, rotational mixing brings hydrogen into the convective core, extending the duration of the MS by up to 15.4 %, averaged over the masses of the evolutionary tracks. When the star begins the helium-burning phase, in the blue loop, we notice an increase in luminosity as rotation increases. Moreover, for stars with $M \leq 5.5 M_\odot$, the extent of the blue loop decreases as the rotation rate increases. On the other hand, for stars with M> 5.5 $M_\odot$, the behavior of the blue loop extension is non-monotonic. During this phase, the rotation rate increases up to the bluest point of the blue loop. At this point, we note that, for models with $\omega_0 \leq 0.7$, the surface rotation rate becomes comparable or even higher than the initial surface rotation rate ω_0. Conversely, for models with $\omega_0 > 0.7$, the rotation rate is always

lower than ω_0. This means that, due to the loss of angular momentum during the H-shell burning phase, it is not possible to observe classical Cepheids with a near-critical rotation rate in this mass range.

In like vein, during the central He-burning phase, multiple "He-spikes" are observed, especially in the tracks between 4 and 5 $M_\odot$. These are associated with uncertainties in the location of the edge of the convective core in the MESA implementation. In the same way, as described in Sweigart & Renzini (1979), small random mixing events, within the semiconvective zone at the edge of the convective core, that move a small amount of helium inwards could produce short-lived loops during the He-burning phase, which are sufficient to produce small increases in PCRs.

When varying the metallicity in our models, we noticed that the lower the metal content, the hotter and more luminous the evolutionary tracks are in general, due to a lower Rosseland mean opacity. However, the behavior of the blue loop is much more complex. Stellar tracks with 4 $M_\odot$ exhibit a monotonic behavior, showing brighter and longer blue loops as the metallicity decreases. For stars with 7 $M_\odot$, $Z = 0.005$, and $\omega_0 > 0.5$, on the other hand, the blue loop is completely suppressed. As expected, the blue loop depends on a multitude of factors, including mass, metallicity, and initial rotation rate.

We use RSP to obtain linear periods at each IS crossing for each stellar track. In addition, the IS edges were also computed using RSP. We do not observe dependencies of IS edges with rotation, but we do observe dependencies with RSP convective parameters. A comparison between sets A, which corresponds to a simple convection model, and C, which adds turbulent pressure and turbulent flux, was performed. We found that the IS obtained with set A contained 94% of classical Cepheids in the LMC from the OGLE-IV catalog. On the other hand, set C contained 87%. Since the convective parameters of set C consider turbulent pressure and turbulent flow, this set is more physically realistic, and was thus adopted for the calculation of linear periods. Calculations with set D, which adds radiative cooling, showed convergence problems.

Linear periods for the fundamental mode were obtained for each evolutionary track

using RSP. Period-age, period-age-temperature, period-luminosity, and period-luminosity-temperature relationships were obtained for three rotation rates and metallicities. The period-age relationships showed dependencies on crossing number, position in the IS, rotation, and metallicity. The period-luminosity relationships became slightly broader with increasing rotation at the second and third crossings. A similar widening is observed when considering a wider range of metallicities.

PCRs were calculated directly from the linear periods. The behavior of the blue loops in the HRD define the shapes of the PCR vs. period diagram. The presence of He-spikes, mainly in tracks with 4 $M_\odot$, produces significant increases in the $\log(dP/dt)$. These irregularities are potentially observable, which would allow us to attribute a physical process to these abrupt changes. First crossing non-rotating models show a higher $\log(dP/dt)$ at the blue end of the IS, while models with a high rotation rate show a higher PCR at the red end of the IS. Models of the second crossing showed a non-monotonic dependence on rotation. On the other hand, non-rotating tracks show a higher PCR during the third crossing. Tracks computed for 5 $M_\odot$ presented a 4th and 5th crossing of the IS. PCRs of the fourth crossing are negative in absolute value and greater by an order of magnitude than the rates of the second crossing. On the contrary, the PCR of the fifth crossing are positive and mixed with those of the third crossing. The typical duration of the fourth crossing is roughly twice the timescale of the first crossing of the IS, while the duration of the fifth crossing is comparable to that of the third crossing of the IS. This implies that a significant number of Cepheids could be in the 5th or even the 4th crossing of the IS. When varying the metal content, models with lower metallicity showed a slight increase in the $\log(dP/dt)$ value during the first crossing. The opposite occurs during the second crossing, where models with higher metallicity present a higher rate. In the case of the third crossing, the behavior is not monotonic with metallicity and shows a dependence on the mass of the star. Models with high mass and $Z = 0.007$ showed a higher rate of change in their respective period range. In contrast, stars with lower mass and $Z = 0.005$ show a higher value of $\log(dP/dt)$. This behavior is attributed to the variations in crossing

timescales and luminosity for each metallicity.

We compared our models with those presented in Anderson et al. (2016). We noticed major differences between $5\,M_\odot$ and $7\,M_\odot$ models, such as ZAMS position, MS extent, RGB temperature, and blue loop behavior. Some of these differences are attributed to differences in the adopted physical parameters, such as mixing length and overshooting, which were solar-calibrated in this work but not in Anderson et al. (2016). However, the differences in the rotation implementation are the most important when comparing the evolutionary tracks. Anderson et al. (2016) presented PCRs for models with $Z = 0.006$. When compared to our values, the positive PCRs are of the same order of magnitude as the values obtained in this work, for models with $Z = 0.007$ and $Z = 0.005$. On the other hand, the negative rates obtained by Anderson et al. (2016) are up to one order of magnitude higher than our $\log(dP/dt)$ values.

Rodríguez-Segovia et al. (in prep.) recently measured PCRs for a sample of 1303 LMC classical Cepheids. Comparing their values with those predicted by our models, a good agreement is observed. Models with $Z = 0.007$ do not cover the short-period data and present a lower value of $\log(dP/dt)$ than those observed in the data from the second crossing. The inability to cover the short period region occupied by the models with $Z = 0.007$ is caused by two main reasons. First, the input physics adopted does not allow blue loops to form in models with mass less than $4\,M_\odot$. Second, the blue edge of the IS, calculated with RSP, is too cold due to the choice of convective parameters, as can be seen in Figure 4.2. PCRs in the short-period region are covered by models with $Z = 0.005$ and $Z = 0.009$. On average, 72.2% of the data fall within 3-sigma of the models. A large part of the data sample are classical Cepheids with implied masses near and below $4\,M_\odot$, with a wide variety of possible initial rotation rates. A small number of data points are consistent with Cepheids of masses greater than $7\,M_\odot$, making them interesting objects for further study, given the scarcity of well-studied Cepheids at the high-mass end of the distribution.

We conclude with a discussion of some of the caveats and plans for future work. Phenomena such as overshooting were simplified in this work by assuming that the over-

shooting parameter is the same in the envelope and in the core. As future work, a calibration of the overshooting parameter in the core should be performed. Besides, physical processes such as pulsation-driven mass loss are not currently implemented in MESA, and this could have an important impact on the PCRs (Neilson & Lester 2008). In order to improve the determination of the IS edges, a study of convective parameters that reproduce an IS that covers all the classical Cepheids from the OGLE catalog of variable stars should be performed. A grid covering a wider range in masses and metallicity would help us cover a wider range of periods and PCRs, better matching the empirical data presented by Rodríguez-Segovia et al. (in prep.). In addition, there is a degeneracy in these models since a PCR vs. period curve with a certain mass, metallicity, and initial rotation rate can be overlapped by a curve with a different combination of these parameters.

Bibliography

Alcock C., et al., 1996, ApJ, 461, 84

Anders E., Grevesse N., 1989, Geochimica Cosmochimica Acta, 53, 197

Anderson R. I., Ekström S., Georgy C., Meynet G., Mowlavi N., Eyer L., 2014, A&A, 564, A100

Anderson R. I., Saio H., Ekström S., Georgy C., Meynet G., 2016, A&A, 591, A8

Angulo C., 1999, in Experimental Nuclear Physics in Europe: Facing the next millennium. pp 365–366, doi:10.1063/1.1301821

Arnett W. D., Meakin C., Viallet M., Campbell S. W., Lattanzio J. C., Mocák M., 2015, ApJ, 809, 30

Asplund M., Grevesse N., Sauval A. J., 2005, in Barnes Thomas G. I., Bash F. N., eds, Astronomical Society of the Pacific Conference Series Vol. 336, Cosmic Abundances as Records of Stellar Evolution and Nucleosynthesis. p. 25

Asplund M., Grevesse N., Sauval A. J., Scott P., 2009, ARA&A, 47, 481

Asplund M., Amarsi A. M., Grevesse N., 2021, arXiv e-prints, p. arXiv:2105.01661

Bahcall J. N., Basu S., Pinsonneault M., Serenelli A. M., 2005, ApJ, 618, 1049–1056

Basu S., Antia H. M., 2004, ApJ, 606, L85

Bélopolsky A., 1895, ApJ, 1, 160

Bergemann M., Serenelli A., 2014, GeoPlanet: Earth and Planetary Sciences, p. 245–258

Blöcker T., 1995, A&A, 297, 727

Bono G., Marconi M., Cassisi S., Caputo F., Gieren W., Pietrzynski G., 2005, ApJ, 621, 966

Cantiello M., Langer N., 2010, A&A, 521, A9

Castelli F., Kurucz R., 2003, in Piskunov N., Weiss W., Gray D., eds, Vol. 210, Modelling of Stellar Atmospheres. p. A20 (arXiv:astro-ph/0405087)

Catelan M., Smith H. A., 2015, Pulsating Stars. Wiley-VCH, Weinheim

Chaboyer B., Fenton W. H., Nelan J. E., Patnaude D. J., Simon F. E., 2001, ApJ, 562, 521

Chandler S. C., 1888, The Astronomical Journal, 8, 81

Chandler S. C., 1896, The Astronomical Journal, 16, 145

Charbonnel C., Zahn J. P., 2007, A&A, 467, L15

Choi J., Dotter A., Conroy C., Cantiello M., Paxton B., Johnson B. D., 2016, ApJ, 823, 102

Claret A., 2007, A&A, 475, 1019

Constantino T., Campbell S. W., Lattanzio J. C., 2017, MNRAS, 472, 4900

Cox A. N., 1980, ARA&A, 18, 15

Cox J. P., Whitney C., 1958, ApJ, 127, 561

Eddington A., 1918, MNRAS, 79, 2

Eddington A., 1919, MNRAS, 79, 177

Eddington A. S., 1924, MNRAS, 84, 308

Eggenberger P., Meynet G., Maeder A., Hirschi R., Charbonnel C., Talon S., Ekström S., 2008, Ap&SS, 316, 43

Eggleton P. P., Dearborn D. S. P., Lattanzio J. C., 2006, Science, 314, 1580

Ekström S., et al., 2012, A&A, 537, A146

Endal A. S., Sofia S., 1976, ApJ, 210, 184

Endal A. S., Sofia S., 1978, ApJ, 220, 279

Evans N. R., et al., 2018, ApJ, 866, 30

Ferguson J. W., Alexander D. R., Allard F., Barman T., Bodnarik J. G., Hauschildt P. H., Heffner-Wong A., Tamanai A., 2005, ApJ, 623, 585

Gallenne A., et al., 2019, A&A, 622, A164

Georgy C., et al., 2013, A&A, 558, A103

Grevesse N., Noels A., 1993, Physica Scripta, T47, 133

Grevesse N., Sauval A. J., 1998, Space Sci. Rev., 85, 161

Grindlay J., Tang S., Los E., Servillat M., 2011, Proceedings of the International Astronomical Union, 7, 29–34

Hauschildt P. H., Allard F., Baron E., 1999a, ApJ, 512, 377

Hauschildt P. H., Allard F., Ferguson J., Baron E., Alexander D. R., 1999b, ApJ, 525, 871

Heger A., Langer N., 2000, ApJ, 544, 1016

Heger A., Langer N., Woosley S. E., 2000, ApJ, 528, 368

Henyey L., Vardya M. S., Bodenheimer P., 1965, ApJ, 142, 841

Herwig F., 2000, A&A, 360, 952

Higl J., Müller E., Weiss A., 2021, A&A, 646, A133

Iglesias C. A., Rogers F. J., 1993, ApJ, 412, 752

Iglesias C. A., Rogers F. J., 1996, ApJ, 464, 943

Jacyszyn-Dobrzeniecka A. M., et al., 2016, Acta Astron., 66, 149

Kippenhahn R., Smith L., 1969, A&A, 1, 142

Kippenhahn R., Thomas H. C., 1970, in Slettebak A., ed., IAU Colloq. 4: Stellar Rotation. p. 20

Kippenhahn R., Weigert A., 1994, Stellar Structure and Evolution. Springer

Kippenhahn R., Ruschenplatt G., Thomas H. C., 1980, A&A, 91, 175

Kramers H. A., 1923, The London, Edinburgh, and Dublin Philosophical Magazine and Journal of Science, 46, 836

Langer N., 1998, A&A, 329, 551

Langer N., Fricke K. J., Sugimoto D., 1983, A&A, 126, 207

Leavitt H. S., 1908, Annals of Harvard College Observatory, 60, 87

Leavitt H. S., Pickering E. C., 1912, Harvard College Observatory Circular, 173, 1

Ludwig H.-G., Freytag B., Steffen M., 1999, A&A, 346, 111

Madore B. F., Freedman W. L., Moak S., 2017, ApJ, 842, 42

Maeder A., Meynet G., 2000, ARA&A, 38, 143

Magic Z., Weiss A., Asplund M., 2015, A&A, 573, A89

Mamajek E., et al., 2015, arXiv, p. 7674

Meynet G., Maeder A., 1997, A&A, 321, 465

Meynet G., Maeder A., 2000, A&A, 361, 101

Michaud G., Fontaine G., Beaudet G., 1984, ApJ, 282, 206

Miller C. L., Neilson H. R., Evans N. R., Engle S. G., Guinan E., 2020, ApJ, 896, 128

Neilson H. R., Lester J. B., 2008, ApJ, 684, 569

Neilson H. R., Langer N., Engle S. G., Guinan E., Izzard R., 2012, ApJ, 760, L18

Neilson H. R., Percy J. R., Smith H. A., 2016, JAAVSO, 44, 179

Nelder J. A., Mead R., 1965, The Computer Journal, 7, 308

Nidever D. L., et al., 2020, ApJ, 895, 88

Nijland A. A., 1903, Astronomische Nachrichten, 161, 229

Paczynski B., et al., 1994, arXiv e-prints, pp astro–ph/9411004

Paquette C., Pelletier C., Fontaine G., Michaud G., 1986, ApJS, 61, 177

Pasetto S., Chiosi C., Cropper M., Grebel E. K., 2016, IAU Focus Meeting, 29B, 747

Paxton B., Bildsten L., Dotter A., Herwig F., Lesaffre P., Timmes F., 2011, ApJS, 192, 3

Paxton B., et al., 2013, ApJS, 208, 4

Paxton B., et al., 2015, ApJS, 220, 15

Paxton B., et al., 2018, ApJS, 234, 34

Paxton B., et al., 2019, ApJS, 243, 10

Pilecki B., et al., 2018, ApJ, 862, 43

Pinsonneault M. H., Kawaler S. D., Demarque P., 1990, ApJS, 74, 501

Planck Collaboration et al., 2020, A&A, 641, A6

Potekhin A. Y., Chabrier G., 2010, Contributions to Plasma Physics, 50, 82

Potter A. T., Tout C. A., Eldridge J. J., 2012, MNRAS, 419, 748

Reimers D., 1975, Memoires of the Societe Royale des Sciences de Liege, 8, 369

Riess A. G., Casertano S., Yuan W., Macri L. M., Scolnic D., 2019, ApJ, 876, 85

Ritter A., 1879, Annalen der Physik, 244, 157

Rogers F. J., Nayfonov A., 2002, ApJ, 576, 1064

Salaris M., Groenewegen M. A. T., Weiss A., 2000, A&A, 355, 299

Saumon D., Chabrier G., van Horn H. M., 1995, ApJS, 99, 713

Shapley H., 1914, ApJ, 40, 448

Silva Aguirre V., Ballot J., Serenelli A. M., Weiss A., 2011, A&A, 529, A63

Skowron D. M., et al., 2021, ApJS, 252, 23

Smolec R., 2009, PhD thesis, Nicolaus Copernicus Astronomical Center, Warsaw, Poland

Smolec R., Moskalik P., 2008, Acta Astron., 58, 193

Soszynski I., et al., 2008, Acta Astron., 58, 163

Soszyński I., et al., 2015, Acta Astron., 65, 297

Soszyński I., et al., 2020, Acta Astron., 70, 101

Stancliffe R. J., Fossati L., Passy J. C., Schneider F. R. N., 2016, A&A, 586, A119

Sweigart A. V., Renzini A., 1979, A&A, 71, 66

Thoul A. A., Bahcall J. N., Loeb A., 1994, ApJ, 421, 828

Timmes F. X., Swesty F. D., 2000, ApJS, 126, 501

Turner D. G., 1996, Journal of the Royal Astronomical Society of Canada, 90, 82

Turner D. G., Abdel-Sabour Abdel-Latif M., Berdnikov L. N., 2006, PASP, 118, 410

Turner D. G., Kovtyukh V. V., Usenko I. A., Gorlova N. I., 2013, ApJ, 762, L8

Ulrich R. K., 1972, ApJ, 172, 165

Valle G., Dell'Omodarme M., Prada Moroni P. G., Degl'Innocenti S., 2019, A&A, 623, A59

VandenBerg D. A., Bergbusch P. A., Dowler P. D., 2006, ApJS, 162, 375

Vogel H. C., 1890, Astronomische Nachrichten, 123, 289

Walmswell J. J., Tout C. A., Eldridge J. J., 2015, MNRAS, 447, 2951

Woo J.-H., Demarque P., 2001, AJ, 122, 1602

Wood T. S., Garaud P., Stellmach S., 2013, ApJ, 768, 157

Xu H. Y., Li Y., 2004a, A&A, 418, 213

Xu H. Y., Li Y., 2004b, A&A, 418, 225

Zahn J. P., 1992, A&A, 265, 115

Zhevakin S., 1953, Astronomicheskii Zhurnal, 30, 161

von Zeipel H., 1924, MNRAS, 84, 665